

Aero-optical properties of subsonic, turbulent boundary layers

**STANISLAV GORDEYEV, JACOB A. CRESS
AND ERIC J. JUMPER**

Aerospace and Mechanical Engineering Department, University of Notre Dame,
Notre Dame, IN 46556, USA

(Received ?? and in revised form ??)

This paper gives the most-complete characterization to date of the optical aberrations imposed on a laser beam propagated through a subsonic, compressible, turbulent boundary layer in a zero-pressure environment, over a range of oblique propagation angles and Mach numbers. This characterization is based on optical measurements made over a number of years using optical-wavefront-sensing instruments that have only become available in the last decade. The primary instrument used in these studies is a Malley Probe, whose method of operation is reviewed here. In general the aberrations imposed by a boundary layer are small, exacerbating the signal-to-noise issues associated with making optical measurements; as such, our approach to dealing with contaminations in these data is discussed in detail. The optical characterization includes optical-wavefront slope spectra, convective velocities and correlation lengths in both stream-wise and cross-stream directions, as well as root-mean-square Optical Path Difference levels. The universality of these characterizations is demonstrated through scaling laws that are introduced using theoretical arguments based on the two most-sited mechanisms for causing the aberrations. The adapted scaling laws have been shown to collapse optical data collected in a number of facilities. Finally, the paper discusses the remaining issues that must be ad-

dressed in order to fully understand the cause of optical aberrations imposed by subsonic turbulent boundary layers.

1. Introduction

When a collimated laser beam propagates through a turbulent compressible flow, different parts of its wavefront travel at different speeds and the wavefront becomes aberrated, as the local speed of light, u , is a function of the local index-of-refraction, n , $u/c = 1/n$, where c is the speed of light in a vacuum. The index-of-refraction in turn depends on the media density, ρ , via a Gladstone–Dale relation, (Gladstone & Dale 1863).

$$(n - 1) = n' = K_{\text{GD}}\rho', \quad (1.1)$$

where ρ' is the density fluctuation and K_{GD} is a Gladstone–Dale constant. This constant depends on the gas mixture and the laser wavelength (Gariner Jr., Hidaka & Tanzawa 1980); for air in the visible wavelength range, K_{GD} is approximately $2.27 \cdot 10^{-4} \text{ m}^3 \text{ kg}^{-1}$.

These optical aberrations caused by either density fluctuations present in the atmosphere (known as the *atmospheric-propagation* problem (Tatarski 1961)) or inside a relatively-thin region of turbulent flow, comprised of compressible shear layers, wakes and turbulent boundary layers around an airborne platform (known as the *aero-optic* problem (Gilbert & Otten 1982)) can severely degrade the performance of an airborne laser system, be it free-space communication, interrogation, targeting or a direct energy application. The impact of these degrading effects can be quantified in different ways; however one of the most common is to quantify it in terms of a time-averaged Strehl ratio, S_t , defined as time-averaged ratio of the actual on-axis intensity at the target, \bar{I} , to the distortion-free, diffraction-limited intensity, I_o , $S_t = \bar{I}/I_o$.

When the propagation length is relatively short, the levels of wavefront distortions can be quantified by Optical Path Length, $OPL(x, y, t)$,

$$OPL(x, y, t) = \int_{z_1}^{z_2} n'(x, y, z, t) dz = K_{GD} \int_{z_1}^{z_2} \rho'(x, y, z, t) dz, \quad (1.2)$$

where the integration is performed along the beam propagation axis, z , and spatial distributions are given on a (x, y) -plane normal to the z -axis. A spatially-averaged mean is commonly subtracted from OPL and defined as Optical Path Difference, $OPD(x, y, t) = OPL(x, y, t) - \langle OPL(x, y, t) \rangle$, where square brackets denote the spatial averaging in the (x, y) -plane.

In recent years, most of the work in aero-optics has been on the aberrating effects of separated shear layers, as they have been shown to be the most aberrating flows; however, the first work in aero-optics was actually for turbulent boundary layers (Jumper & Fitzgerald 2001). The first work in this area was a theoretical study by Liepmann (1952) and published as a Douglas Aircraft Company Technical Report and made use of the jitter angle of a thin beam of light as it traveled through the compressible boundary layer on the sides of high-speed wind tunnels as a way to quantify the crispness of Schlieren photographs. A significant piece of work was done by Stine & Winovich (1956); they performed photometric measurements of the time-averaged radiation field at the focal plane of a receiving telescope in an attempt to validate Liepmann’s formulations. Their work brought together all that had been done till then on optical propagation through index-variant turbulent flows. Their work also raised the prospect of using an optical degradation measurement as a method of inferring turbulence scales. Based heavily on the approach taken by Tatarski (1961) for electromagnetic waves propagated through the atmosphere, in the early 1960’s, Sutton produced the most-widely referred to theoretical formulation for the aberrating effects of turbulent boundary layers based on statistical measures of the turbulence (Liepmann 1952) and developed a “linking equation” between

the turbulence quantities and the optical phase variance (Sutton 1969),

$$\sigma_\phi^2 = 2K_{\text{GD}}^2 k^2 \int_0^L \rho_{\text{r.m.s.}}(y)^2 \Lambda_\rho(y) dy, \quad (1.3)$$

where σ_ϕ is the phase variance, $\rho_{\text{r.m.s.}}$ is the root-mean-square density and $\Lambda_\rho(y)$ is the density correlation length in the wall-normal direction. The phase variance, σ_ϕ , is related to the OPD variance through the wavenumber, $k = 2\pi/\lambda$, by $\sigma_\phi = \text{OPD}_{\text{r.m.s.}} k$, where λ is the laser wavelength.

Interestingly, by incorporating the realization first reported by Malley, Sutton & Kinchloe (1992) that aberrations produced by a laser propagated through convecting flow structures themselves convect, it can be shown that both Liepmann's and Sutton's formulations are identical (Jumper & Fitzgerald 2001). Due to the same motivation that produced (1.3), work on the turbulent boundary layer intensified in the late 1960's and through the decade of the 1970's due to an interest in placing lasers on aircraft. In the 1970's, Rose (1979) conducted the most extensive, at that time, experimental studies of optical aberrations caused by a turbulent boundary layer. He conducted hotwire measurements in turbulent boundary layers in order to indirectly obtain their density fluctuations, $\rho'(y)$, (assuming that pressure fluctuations inside the boundary layer were zero) and associated correlation lengths, $\Lambda_\rho(y)$. These were used to estimate wavefront aberrations that would be imprinted on a laser beam propagated through the same turbulent boundary layer assuming homogeneous turbulence. The on-average wavefront aberrations, in the form of $\text{OPD}_{\text{r.m.s.}}$, (the time-averaged spatial root-mean-square of OPD) were estimated using Sutton's linking equation (1.3). Rose empirically found $\text{OPD}_{\text{r.m.s.}}$ to be *proportional* to dynamic pressure, q , and boundary layer thickness, δ , such that $\text{OPD}_{\text{r.m.s.}} \sim q\delta$.

These aircraft hotwire measurements were complemented by the work of Gilbert (1982), who performed interferometer measurements. In the Gilbert work, the interferometry

used a double-pulse technique, which measured the difference in the wavefront from one pulse to another, rather than the distorted wavefront at a given instant, and only a limited number of these were made. Gilbert reported that the interferometry *generally* supported the hotwire, integral-method estimations of the $\text{OPD}_{\text{r.m.s.}}$; however, based on his work, Gilbert concluded that the *square* of the $\text{OPD}_{\text{r.m.s.}}$ depended *linearly* on the dynamic pressure, $\text{OPD}_{\text{r.m.s.}}^2 \sim q$.

A review of the major publications in aero-optics (Gilbert & Otten 1982) from the 1970's demonstrates that work up until 1982 focused on the measurement of the time-averaged, spatial, near-field optical phase variance, σ_ϕ^2 , either by direct optically-based methods, or assessed indirectly using fluid-mechanic measurements via the linking equation (1.3). Optical methods of that time that have been applied to the measurement of the near-field time-averaged phase variance include direct interferometry, pulsed interferometry, and shearing interferometry. These interferometric methods provided a time-averaged assessment of the optical phase variance over the aperture; however, these methods provided no information concerning temporal frequencies.

Masson, Wissler & McMackin (1994) revisited the Gilbert and Rose data and concluded that after removing systematic errors from Gilbert's data, $\text{OPD}_{\text{r.m.s.}} \sim (\rho M^2)^{1.16}$. He also found that there appeared to be a systematic difference between direct and indirect wavefront error measurements, with the interferometric estimates consistently yielding higher estimates of the $\text{OPD}_{\text{r.m.s.}}$ than the hotwire estimates, but could not offer a reasonable explanation why optical and hotwire data did not agree in magnitude. The appearance of the Masson *et al.* (1994) paper revisiting data taken through the early 1980's is evidence that interest/funding in aero-optics had long come to an end. In fact, Sutton (1985) announced that aero-optics was a mature discipline requiring only the measurement of the turbulence statistics of a few additional flows.

In the 1990's these arguments were revisited based on the fact that newer lasers envisioned for airborne platforms were an order of magnitude shorter wavelength than those of the 1970's and 1980's. In the 1970's and 1980's the airborne laser system of the day was the Airborne Laser Laboratory, ALL, which used a CO₂ laser with a wavelength of 10.6 μm . The typical level of optical aberrations caused by the boundary layer is $\text{OPD}_{\text{r.m.s.}} \sim 0.1 \mu\text{m}$, and at this wavelength, it would reduce the Strehl ratio by less than 1%. This estimation is based on the large aperture approximation (Smith 1966) for the fraction of diffraction-limited intensity on target based on the $\text{OPD}_{\text{r.m.s.}}$ and laser wavelength, λ , as

$$\overline{S}_t = \exp \left[- \left(\frac{2\pi \text{OPD}_{\text{r.m.s.}}}{\lambda} \right)^2 \right]. \quad (1.4)$$

Notice that the exponent scales as $(1/\lambda)^2$. Wavelengths of interest in modern optical systems are in the near-IR ($\sim 1 \mu\text{m}$) and visible spectrum. Thus, the $\text{OPD}_{\text{r.m.s.}}$ predicted by Gilbert and Rose ($\sim 0.1 \mu\text{m}$) that were known to be inconsequential at the wavelength of 10.6 μm , now drop the Strehl ratio by about 30% or more. As such, there is now a renewed interest in revisiting the turbulent boundary layer problem.

Also, there now exist direct optical instrumentation capable of assessing not only the $\text{OPD}_{\text{r.m.s.}}$, but also the spatial and temporal frequencies of the aberrations, and, as will be described below, the ability to construct wavefronts from which the far-field intensity pattern can be computed directly. Using the time-resolved time series of far-field patterns, Strehl ratio as a function of time can be computed. From the point of view of applications to free-space communication, which are concerned with bit error rate, these time series of instantaneous Strehl ratio are more instructive than their average. However, once the time series are available, the time-averaged Strehl ratio can be computed, which is of interest to directed energy applications that depend only on maintaining an average intensity above some critical threshold.

Finally, because conformal windows (which presume an attached turbulent boundary layer), as opposed to beam-directing turrets (which require beam propagation through regions of separated flow), are now being considered for exit pupils, it is critical that a more reliable method of predicting the turbulent boundary layer's aberration character is needed. Not only is it important to measure the aero-optical effects of the turbulent boundary layer for propagation normal to the boundary layer, it is now possible, and of interest to measure its effects at all relevant oblique angles. In addition, with the new ability to obtain direct, high-fidelity optical data without resorting to indirect methods of predicting the optical aberrations, it is now more efficient to revisit the question of scaling of the aero-optic data.

The pioneering use of a new wavefront device called a Malley probe in making optical measurements in turbulent boundary layers (Gordeyev, Jumper, Ng & Cain 2003) has shown to give the most accurate and highly time-resolved information about optical distortions (bandwidths > 100 kHz). It was found (Wittich, Gordeyev & Jumper 2007) that optical distortions were proportional to the boundary layer thickness, the freestream density and the square of the freestream Mach number, $OPD_{r.m.s.} \sim \delta \rho M^2$, which is consistent with the finding by Rose (1979), but not with Gilbert (1982) or Mason *et al.* (1994). It was also found that optical distortions convect at speeds of 0.82–0.85 of the freestream speed, which suggest that optically-active structures reside in the outer portion of the boundary layer.

To our knowledge the only other experimental investigations of optical distortions caused by turbulent boundary layers since the work of the 1980's and 1990's was the study at Princeton (Wyckham, Zaidi, Miles & Smits 2005). That study made use of a high-speed camera to make a high-bandwidth Shack Hartmann Sensor and then apply it to the investigation of transonic and supersonic boundary layers with and without surface

injection of various gases. Unfortunately the signal-to-noise ratio of the sensor introduced much uncertainty into their results and conclusions drawn from them. Regardless of the uncertainty in their results, they proposed a scaling law that was based on a model that presumed that the pressure fluctuations in the boundary layer are negligible, invoking the “Strong Reynolds Analogy,” (Morkivin 1962) which has now been conclusively shown to be incorrect in the case of shear layers (Fitzgerald & Jumper 2004), but as will be discussed later in this paper, remains an open question for turbulent boundary layers. What is interesting is the fact that the scaling based on $OPD_{r.m.s.} \sim \delta^* \rho M^2$ still comes out of their analysis, so that scaling laws alone cannot be used to discriminate between the two proposed mechanisms: temperature-driven fluctuations versus pressure wells inside vortical structures. We will return to this discussion later in Section 5.

Because of great challenges in accurately computing a time-resolved, compressible boundary layer at high transonic Mach numbers, only few attempts to numerically compute optical aberrations inside turbulent boundary layers have been made. Truman & Lee (1990) and Truman (1992) used a DNS spectral method to calculate time-dependent optical distortions for a low-Reynolds-number boundary layer, where the density fluctuations were computed from temperature fluctuations due to temperature being transported as a passive scalar under the assumption of constant pressure. Large-scale streamwise elongated regions of highly-correlated optical distortions were found and the link between highly anisotropic hairpin vortical structures leading to the optical distortions were observed. It was also found that the optical distortions were anisotropic and vary significantly with the propagation (elevation) angle. Tromeur, Garnier, Sagaut & Basdevant (2002, 2003) and Tromeur, Garnier & Sagaut (2006*b*) calculated optical aberrations caused by a compressible turbulent boundary layer at subsonic ($M = 0.9$) and supersonic ($M = 2.3$) speeds for $Re_\theta = 2917$ using large-eddy simulations, LES, which compared

favourably with some limited experimental data (Deron, Tromeur, Aupoix & Desse 2002). They found that the optical aberrations traveled at 0.8 of the freestream speed and were dominated by large-scale structures residing in the outer portion of the boundary layer. They also questioned the applicability of the Sutton model (1.3) for boundary layers (Tromeur, Garnier & Sagaut 2006*a*).

The purpose of this paper is to present the results of comprehensive experimental studies of the aero-optical effects through high-Mach-number, subsonic turbulent boundary layers over a range of boundary layer thicknesses, freestream Mach numbers and oblique propagation angles. But it should be noted that publication of this paper has been delayed, until we felt comfortable that we have properly addressed the issues of accuracy and repeatability. Our first meeting paper (Gordeyev *et al.* 2003) on the optical character of high-subsonic turbulent boundary layers was in 2003. The results from that paper are referred to in the present paper; however, it has taken these many years to assure ourselves that the data included in this paper and conclusions drawn from them will not change appreciably with the continued advance in instruments and techniques. As mentioned previously, these conclusions are heavily dependent on the use of the Malley Probe; however, much effort has been made to make direct comparison of the Malley Probe results with other instruments used to interrogate the same flows. Further, as will become clear in this paper, accurate and repeatable data required the development of techniques for increasing signal-to-noise ratios and methods of removing corrupting influences as well as understanding the effect of aperture size on suppression or proper filtering of the data. We now believe that these issues of accuracy and repeatability have been sufficiently addressed to draw the conclusions presented here.

As the results in this paper depend on the instruments used, Section 2 describes the optical sensor used to collect much of the data, the Malley probe, which is capable of

accurately measuring small levels of optical aberrations and their average convective speeds. The paper then continues in Section 3 to describe the experimental setups used for the boundary layer studies. Section 4 presents and discusses the results of the optical measurements, including measured auto-correlations and length scales of optical aberrations. A model using Strong Reynolds Analogy and a separate vortical-structure model are proposed and discussed; both models are shown to provide a correct scaling law for the experimental results, as well as other experimentally observed results. In Section 5, different contributors to the physical mechanism of optical distortions are discussed.

2. Malley probe

The Malley Probe is an optical sensor based upon the technique introduced by Malley *et al.* (1992). The operation of this instrument is described in Gordeyev, Hayden & Jumper (2007); however, as an understanding of its operation is needed to interpret some of the data, some essential details are repeated here. The principle of the Malley probe operation relies on Huygens' Principle that a small-aperture beam that passes through a variable-index-of-refraction field, will emerge from that region perpendicular to the wavefront of a larger beam propagated through the same flow at the same instance. Measuring the resulting deflection angle of a small-aperture beam, θ , is equivalent to measuring the slope of the wavefront (Jumper & Fitzgerald 2001). OPD, or relative wavefront, can be found by integrating the wavefront slope,

$$\text{OPD}(x) = \int_0^x \frac{d\text{OPD}}{dx} dx. \quad (2.1)$$

For unchanging, convecting aberrations, Malley *et al.* (1992) realized that several closely spaced spatial measurements of the wavefront derivative, could be replaced by a temporal record of the wavefront slope at a single location. The OPD as a function of time then

becomes,

$$\text{OPD}(x_o, t) = \int_0^t \frac{d\text{OPD}(x, t)}{dx} \Big|_{x=x_o} \frac{dx}{dt} dt = -U_c \int_0^t \theta(x, t) \Big|_{x=x_o} dt, \quad (2.2)$$

where $d\text{OPD}(x, t)/dx = -\theta(x, t)$, the time history of deflection angle or jitter, and $U_c = dx/dt$, is the convective velocity of the optical aberrations.

In their original work, Malley *et al.* (1992) used one beam to measure the jitter signal at a single location and the convective velocity of the optical aberrations was estimated based on knowledge of the flow. Gordeyev *et al.* (2007) made use of a second small-aperture laser beam in a manner similar to Hugo & Jumper (1995), but now separated by a small distance from the first one and calculated the convective speed *directly* by cross-correlating deflection angles and finding an average time it takes for optically-active structures to travel from the upstream beam to the downstream beam. Gordeyev *et al.* (2007) compared two optical techniques for measuring the convective velocity with a Malley probe: a *direct method* similar to that used by Hugo & Jumper (1995) and a new *spectral/phase method*. For the direct method, the temporal cross-correlation of the two jitter signals, $\theta_1(t)$ and $\theta_2(t)$, are computed, $R(\tau) = E\{\theta_1(t)\theta_2(t + \tau)\}$, and the (travel) time delay corresponding to a maximum correlation is found, τ^{delay} . Knowing the separation distance between the two beams, Δ , and the time delay to the maximum cross correlation, the convective velocity could be found, $U_c = \Delta/\tau^{\text{delay}}$. Rather than accurately estimating the convection velocity of the aberrating structures in the flow, the direct cross-correlation method was found to be sensitive to signal contamination from beam jitter sources, mechanical vibration of the tunnel walls and optical bench, and electronic noise. To lessen the impact of these contaminants, a spectral method of computing the time delay was developed. The spectral or phase method makes use of the

spectral cross-correlation function,

$$S(f) = \int R(\tau) \exp(-i2\pi f\tau) d\tau = \frac{1}{T} \langle \hat{\theta}_1(f) \hat{\theta}_2^*(f) \rangle, \quad (2.3)$$

where the brackets indicate ensemble averaging, the carrot symbol denotes the Fourier transform and the asterisk is the complex conjugate. Assuming a frozen flow, the optical aberrations will be purely convecting structures; therefore the downstream signal, θ_2 , will be a time-delayed duplicate of the upstream signal, θ_1 : $\theta_2(t) = \theta_1(t - \tau^{\text{delay}})$. Taking the Fourier transform of θ_2 gives $\hat{\theta}_2(f) = \hat{\theta}_1(f) \exp(-i2\pi f\tau^{\text{delay}})$. Using this relationship (2.3), the spectral correlation, $S(f)$, becomes,

$$S(f) = \frac{1}{T} \langle \hat{\theta}_1(f) \left[\hat{\theta}_1(f) \exp(-i2\pi f\tau^{\text{delay}}) \right]^* \rangle = A(f) \exp(i2\pi f\tau^{\text{delay}}), \quad (2.4)$$

where $A(f) = 1/T \langle \hat{\theta}_1(f) \hat{\theta}_1^*(f) \rangle$ is a *real function* of f . The time delay, τ^{delay} , can be found from the argument of the spectral cross-correlation,

$$\tau^{\text{delay}}(f) = \frac{1}{2\pi} \frac{d}{df} \arg[S(f)]. \quad (2.5)$$

As with the direct method, knowing the distance between the upstream and downstream beams, Δ , the convective velocity, $U_c = \Delta/\tau^{\text{delay}}$, can be found. With the spectral method, parts of the spectra corresponding to travelling structures can be easily separated from any stationary contamination (mechanical vibrations, for instance), since the phase difference between two beams at these contaminating frequencies will be zero, while the “traveling” parts of the spectrum will have a linear phase difference with frequency. In addition, with the spectral/phase method, the maximum time delay can be computed over short frequency bins, therefore the convective velocity can also be found as a function of frequency; $U_c(f) = \Delta/\tau^{\text{delay}}(f)$. This frequency-related information is quite helpful, especially in identifying the convective velocities for different regions in the flow field that are associated with distinct frequency bands.

Figure 1 shows a schematic of a typical Malley probe setup. In this configuration,

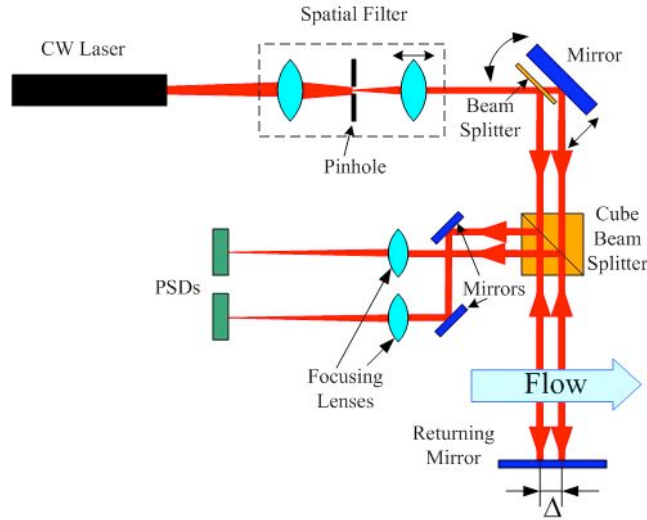


FIGURE 1. Schematic of a typical Malley probe setup.

a CW HeNe laser is spatially filtered and split into two parallel, closely spaced small-aperture (~ 1 mm) beams. The two beams are then passed through the flow field of interest; the beams are aligned in the streamwise or convective direction. The beams are typically reflected off a return mirror back along their original path in order to double the signal-to-noise ratio. Then the beams are split out of the original path using a cube beam splitter and, after separating, are sent through focusing lenses, which remove any contamination from possible lateral beam displacements and leave only the angular deflection component. Finally, the beams are focused onto two highly-sensitive position sensing devices (PSDs) to measure the temporal deflection or jitter of the beams, θ , by measuring the focal spot displacements on the PSDs, d , since $\theta = d/F$, where F is the lens focal length. The deflection angle is recorded at sampling frequencies > 100 kHz for several seconds. From the time-record of the deflection angle of the small-aperture Malley probe beam, a temporal wavefront $OPD(t)$ can be calculated using (2.2). Finally, time is replaced with a streamwise distance using a Taylor frozen flow hypothesis, $x = -U_c t$, and the wavefront as a function of space, $OPD(x)$, can be found.

Since the sampling time can be made arbitrarily large, the resulting measured wavefront can be reconstructed over any streamwise aperture size; assuming the frozen flow hypothesis. To calculate the relevant $OPD_{r.m.s.}$ for a given physical aperture, Ap , the wavefront is apertured and, after removing the piston and tilt component from each apertured wavefront, the resulting $OPD_{r.m.s.}$ can be calculated for each record and ensemble averaged over all records. This procedure of removing tilt is common in beam control systems via fast steering mirrors used to keep the beam aligned; the removal of tilt has been shown to act as a high-pass filter on the wavefront (Siegenthaler, Gordeyev & Jumper 2005). As this filter effect is important to the interpretation of some of the character of the high-frequency content of the beam-jitter spectra, a brief description of it, along with the approach to computing $OPD_{r.m.s.}$ directly from the spectra is included in Section 4.2.2.

3. Experimental setup

Turbulent boundary layer measurements were conducted in wind tunnel facilities at the University of Notre Dame (ND), and at the United States Air Force Academy (US-AFA). These facilities were modified to perform optical measurements of either a single boundary layer (later referred to as single boundary layer measurements or SBL) on one of the tunnel walls or simultaneous optical measurements through two boundary layers on opposite walls of the tunnels (referred to double boundary layer measurements or DBL).

3.1. Notre Dame experimental setup

Optical and flow velocity measurements were taken in one of the indraft, transonic wind tunnels in the University of Notre Dame Hessert Laboratory for Aerospace Research. The tunnel was comprised of an inlet, with a contraction ratio of 150:1, boundary layer

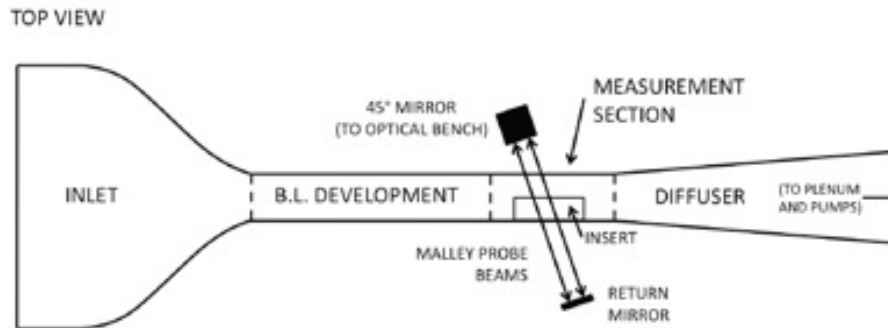


FIGURE 2. Schematic of the Notre Dame turbulent boundary layer test facility.

development section, measurement section, and a diffuser, see Figure 2. The cross-section of the development and measurement sections measured 9.9 cm by 10.1 cm, and were constructed of Plexiglas. The smooth-wall development section had an overall length of 170 cm. The diffuser was connected to a large, gated plenum. Pressure in the plenum was lowered using either one or two vacuum pumps to achieve the desired flow velocity in the test section. Air velocity was controlled by adjusting the rotation rate of the centrifugal vacuum pumps; fine-tuning adjustments were made to the plenum pressure with an auxiliary exhaust valve. The boundary layer development section was designed to allow hotwire access along the tunnel. A linear traverse mechanism could be placed in access ports at thirteen streamwise locations along the length of the development section. At each hotwire measurement location, total and static pressure ports were installed to measure the local Mach number. Hotwire velocity measurements were made at each of the thirteen stations on one wall of the wind tunnel. The optical measurement section had two optical quality glass flats placed on opposite sides of the tunnel. One flat was removable to allow the single boundary layer optical insert to be installed, see Figure 3. Total and static ports were placed just upstream of the optical measurement section. An optical insert was designed and constructed to allow the boundary layer on one wall of the wind tunnel to be optically bypassed. The optical flat was removed from one of the tunnel

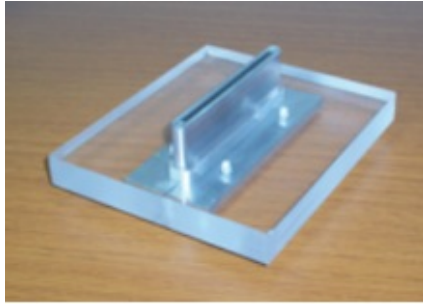


FIGURE 3. Optical insert for the Notre Dame turbulent boundary layer wind tunnel.

walls, and the optical insert, shown in Figure 3, was placed in the opening. The narrow optical insert protruded 25 mm into the flow, was 100 mm in length and 5 mm in width. The insert was of sufficient length that the oblique propagation angle, β , that the Malley Probe beams made with the tunnel's streamwise direction could be varied from 60° to 120° . The insert opening was capped with a transparent Plexiglas plate 3 mm thick. The oblique propagation angle is defined such that 0° is in the upstream direction and 180° is in the downstream direction; wall-normal is 90° . Figure 4 shows schematics for the two wind tunnel test configurations: single and double turbulent boundary layers. Each configuration was tested at four Mach numbers (0.4, 0.5, 0.6 and 0.7) and for several oblique angles (60° , 70° , 80° , 90° , and 110°). To verify that the Malley-probe, one-dimensional wavefronts provided correct average levels of optical aberrations, a limited number of two-dimensional wavefronts were taken using a distorted grating wavefront sensor. The distorted-gratings round laser beam was apertured to 62 mm in diameter and was propagated through both boundary layers at a 90° propagation angle.

3.2. USAFA experimental setup

Optical measurements were also made in the Subsonic Wind Tunnel Facility at the United States Air Force Academy. This closed-loop wind tunnel has a 2.4 m long test section with a cross-sectional area that measures 0.914 m by 0.914 m, see Figure 5. The wind tunnel

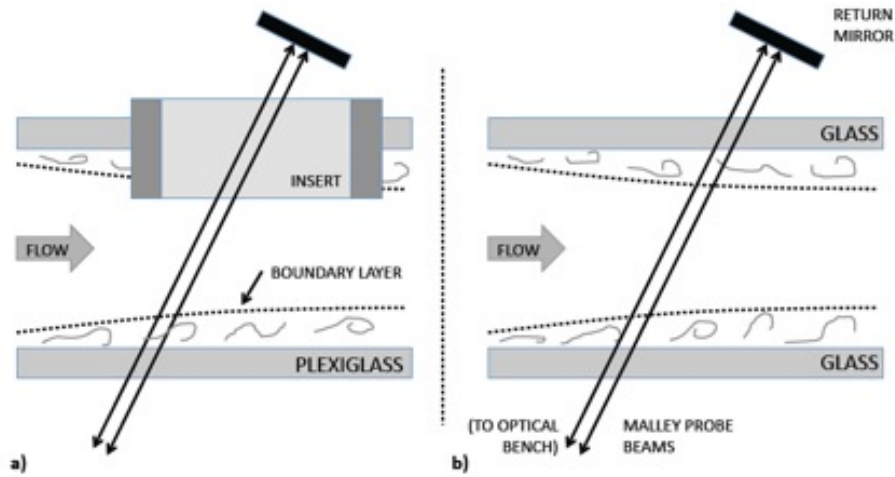


FIGURE 4. Schematics of the measurement section for a) single boundary layer measurements with the optical insert in place to by-pass the boundary layer on one wall; and b) double (two-statistically independent) boundary layer measurements.

could achieve air velocities up to Mach 0.5, but with limited run-time due to drive motor heating. Three Mach numbers were tested, Mach 0.4, 0.45 and 0.5. As with the Notre Dame tests, both single and double turbulent boundary layers were measured, as shown in Figure 4. It was necessary to build a larger optical insert for the thicker boundary layer and larger test section of the USAFA facility. The length of the new optical insert was 250 mm, 6 mm in width and it protruded 40 mm into the test section. The Plexiglas window in the optical insert was 5 mm thick. Due to physical obstructions from the tunnel bracing supports, optical access for the measured elevation angles was slightly different for the single versus double boundary layer tests. For the single boundary layer tests, the measured oblique angles were 48° , 90° , 124° , and 133° . The double boundary layer was measured at oblique angles of 90° , 116° , 126° , 132° , and 140° .

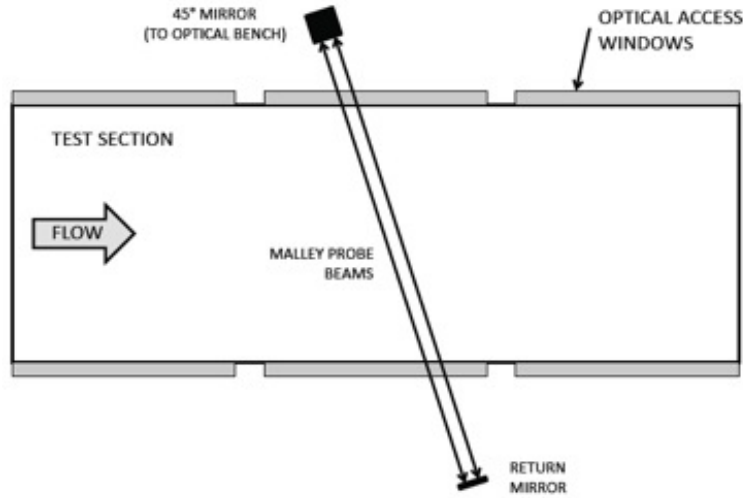


FIGURE 5. Schematics of the United States Air Force Academy Subsonic Wind Tunnel Facility test section.

4. Results

4.1. Hotwire results

The lower wall boundary layer profile in the Notre Dame tunnel was measured with a single boundary layer hotwire at several locations along the streamwise axis of the test section between $x = 13$ cm and $x = 156$ cm; Malley probe measurements were taken at 170 cm downstream of the beginning of the boundary layer section. Mean- and r.m.s.-velocity profiles at 13 streamwise locations along the tunnel wall were measured; as an example typical of all Mach numbers, five of the profiles normalized by the freestream velocity, U_∞ , and local displacement thickness, δ^* , for the Mach number of 0.4 are presented in Figure 6a. It should be noted that all data have been reduced using the displacement thickness rather than the boundary layer thickness to remove subjectivity associated with estimating the boundary layer thickness. The boundary layer profiles exhibited a self-similar behavior after the streamwise location of $x = 15$ cm. The velocity profile at $x = 156$ cm, which is 14 cm upstream of the optical-measurement location, is plotted in

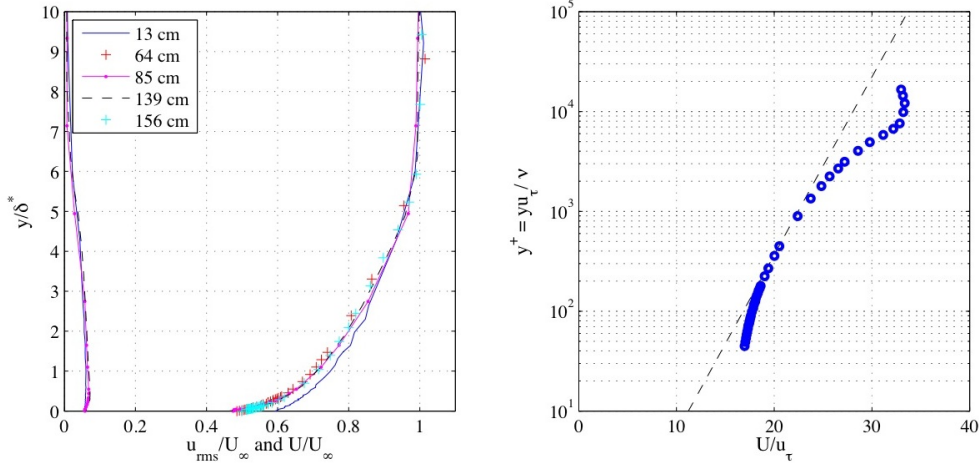


FIGURE 6. a) Normalized hotwire velocity profiles (mean and r.m.s.) of the wall boundary layer in the Notre Dame transonic wind tunnel at 5 streamwise locations for $M = 0.4$ b) Boundary layer profile in inner units 14 cm upstream of the optical measurement section. The friction velocity is 5.5 m s^{-1} . The dashed line represents the log-law, $u^+ = 1/\kappa \log y^+ + B$.

Figure 6b in wall units. The log-law relationship, $u^+ = (1/\kappa) \log y^+ + B$, is also plotted in Figure 6b, with $\kappa = 0.41$ and $B = 5.6$. The freestream Mach number for this profile was 0.5. Using the Clauser method, the friction velocity, u_τ , was found to be 5.5 m s^{-1} . The profile in Figure 6b exhibits a log-law region from $y^+ \sim 200$ to 1000. The boundary layer displacement thickness, δ^* , was 3.6 mm and the momentum thickness, θ , was found to be 2.75 mm. The Reynolds number based on the momentum thickness, $Re_\theta = U_\infty \theta / \nu$, was approximately 35,400 at this station and Mach number and the Reynolds number based on the development length $x = 170 \text{ cm}$, $Re_x = U_\infty x / \nu$, was approximately $21.9 \cdot 10^6$. The shape factor $H = \delta^* / \theta$ for this boundary layer was 1.3, which agrees well with values for zero-pressure-gradient boundary layers (Nagib, Chauhan & Monkewitz 2005) at this Re_θ .

The boundary layer in the USAFA tunnel was measured using a Pitot-probe (Dumas, Fuqua & Hayden 2005). At Mach 0.4, the displacement and momentum thicknesses at the optical measurement location were estimated to be 4.17 mm and 3.32 mm, respectively,

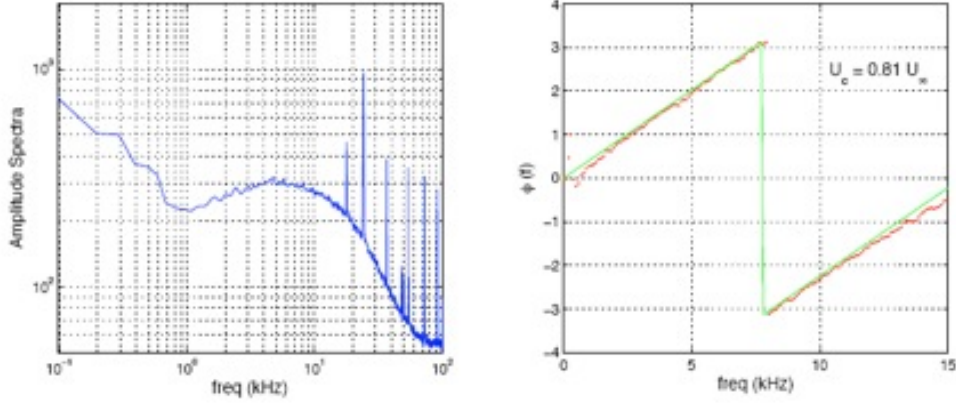


FIGURE 7. a) Jitter amplitude spectrum for Malley probe beams through two boundary layers at $M = 0.4$. b) The corresponding phase angle data (dots) showing the convection velocity of the optical aberrations to be 0.81 of the freestream velocity. The line is a linear curve-fit.

with the corresponding value for $H = 1.26$. Re_θ varied from 34,000 to 42,500 for the Mach number range from 0.4 to 0.5.

4.2. Malley probe results

4.2.1. Wall-normal projection

The first data to be discussed is for normal projection through both the upper- and lower-wall boundary layers of the Notre Dame tunnel (see Figure 4b, DBL case). In this case, the streamwise-aligned, Malley probe beams propagated through two independent boundary layers normal to the tunnel walls. The Malley probe jitter amplitude spectrum, $|\hat{\theta}_1(f)|$, for the Mach 0.4 case is shown in Figure 7a and the associated phase plot, $\arg[S(f)]$, defined in (2.4) is shown in Figure 7b. As will be discussed later, these spectra were representative of all optical measurements in both facilities.

As many spectra will be referred to in this paper, it is worth discussing the character of these data in Figure 7 in some detail. First, the spikes in the spectra in the high-frequency range in Figure 7a are due to electronic and RF noise due to various sources present in the laboratory. Because the PSDs are made from photoelectric materials, the sensor itself

is a current-producing device; the current is converted to voltage via transimpedance amplifiers. As such, electronic noise at specific facility-dependent frequencies is amplified and shows up as spikes. At the low-frequency end of the spectra, vibration corruption from the tunnel and optical bench cause an increase in spectra amplitude at frequencies below 1 kHz. These facility-related vibrations affect both Malley-probe beams simultaneously, i.e. in-phase; as such, the phase plot in Figure 7b shows a flat, approximately zero value at frequencies up to 1 kHz. Above 1 kHz, the phase is a linear function of frequency, as can be seen by the linear line on the phase plot. The jump in the phase plot is due to folding the phase change by 2π . Using (2.5), the linear slope in the phase plot gives a convective velocity for the optical structures to be approximately 0.81 of the freestream velocity. The convective velocity was found to be approximately the same in both ND and USAFA experiments for all Mach numbers tested.

The phase plot in Figure 7b shows the presence of convecting optical structures above 1 kHz. The jitter amplitude spectrum, Figure 7a, shows a “hump” with a maximum occurring at ~ 5 kHz. Assuming that the boundary layer thickness, δ , was approximately $7\delta^*$, $U_c = 119 \text{ m s}^{-1}$ and $f = 5 \text{ kHz}$, the “hump” in the spectra corresponds to a Strouhal number, $St_\delta = f\delta/U_c \approx 1$, suggesting that the most significant optical aberrations are on the order of the boundary layer thickness in the streamwise direction. Also, the optically aberrating structures move at a relatively-high convective speed of 0.81. Taken together, these results suggest that the most relevant aberrating structures in the boundary layer reside in the outer portion of the boundary layer, $y^+ > 1000$ or $y/\delta^* > 0.7$ (see Figure 6a). In order to further reduce the optical data the corruptions discussed earlier have to be removed.

4.2.2. Relationship between deflection-angle spectra and $\text{OPD}_{\text{r.m.s.}}$

The rise in the spectra at frequencies below 1 kHz is due to mechanically-induced vibrations. In order to remove this mechanical-vibration corruption, one needs to know the correct, uncorrupted behavior of the deflection-angle spectrum at the low-frequency end to properly filter it out.

To derive a proper high-pass filter, it is helpful to review how Malley probe one-dimensional jitter/deflection-angle amplitude spectra, $P_\theta(f) = \langle \hat{\theta}(f)\hat{\theta}^*(f) \rangle$, are related to $\text{OPD}_{\text{r.m.s.}}$ for a given large-aperture aperture size, Ap . These quantities are related as follows: since OPD is the conjugate of the wavefront, $\text{OPD}_{\text{r.m.s.}}^2 \equiv W_{\text{r.m.s.}}^2$, the $\text{OPD}_{\text{r.m.s.}}$ is related to the 1-D wavefront power spectrum, $P_W(k) = \langle \hat{W}(k)\hat{W}^*(k) \rangle$, as,

$$\text{OPD}_{\text{r.m.s.}}^2 \equiv \frac{1}{2\pi} \int_{-\infty}^{\infty} P_W(k)dk = \int_{-\infty}^{\infty} P_W(f)df, \quad (4.1)$$

where $\hat{W}(k)$ is the Fourier transform of a 1-D wavefront distortion, $W(x)$. But the jitter/deflection angle, θ , is the spatial derivative in the streamwise direction of the wavefront,

$$\theta(x = -U_c t) = \frac{dW(x = -U_c t)}{dx} = -\frac{1}{U_c} \frac{dW(t)}{dt}. \quad (4.2)$$

As mentioned earlier, the frozen-flow convective hypothesis is applied with U_c being the convective speed. So, the wavefront power spectrum can be computed from the deflection angle power spectrum, as $P_W(f) = [U_c/(2\pi f)]^2 P_\theta(f)$. Substituting (4.2) into (4.1) we get,

$$\text{OPD}_{\text{r.m.s.}}^2 = \int_{-\infty}^{\infty} P_W(f)df = \int_{-\infty}^{\infty} \left(\frac{U_c}{2\pi f} \right)^2 P_\theta(f)df = U_c^2 \int_{-\infty}^{\infty} \frac{P_\theta(f)}{(2\pi f)^2} df. \quad (4.3)$$

The derived expression is valid only for an infinite aperture. As mentioned earlier, placing an aperture on the beam and removing tip/tilt acts as a filter. In Siegenthaler *et al.* (2005), it was shown that for finite apertures, the above expression should be

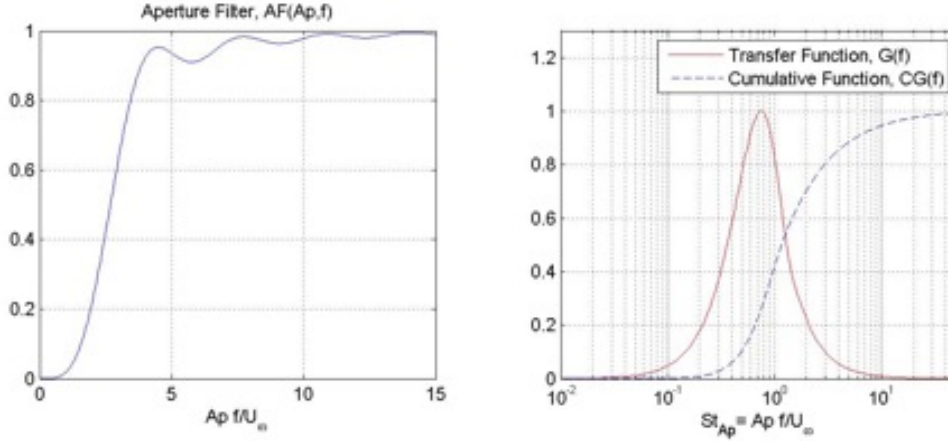


FIGURE 8. a) Aperture filter. b) Optical transfer and cumulative functions.

modified by including a one-dimensional aperture filter, $AF(Ap, f)$, see Figure 8a,

$$OPD_{r.m.s.}^2(Ap) = U_c^2 \int_{-\infty}^{\infty} AF(Ap, f) \frac{P_\theta(f)}{(2\pi f)^2} df = \int_0^{\infty} G(Ap, f) P_\theta(f) df, \quad (4.4)$$

where $G(Ap, f) = 2[U_c/(2\pi f)]^2 AF(Ap, f)$ is a transfer function between the deflection angle spectrum and the apertured $OPD_{r.m.s.}(Ap)$. Figure 8b, shows the transfer function, $G(f)$, normalized by its maximum value as a function of $St_{Ap} = fAp/U_\infty$. The normalized cumulative transfer function, $CG(f) = \int_0^f G(x)dx / \int_0^\infty G(x)dx$, is also plotted in Figure 8b. The transfer function is essentially a band-pass filter, centered around $St_{Ap} = 0.8$. The low-frequency cut-off is due to aperture effects; for most beam-alignment systems the very low frequencies are present essentially as tip/tilt and are normally removed by a Fast Steering Mirror. The high-frequency cut-off is due to the integral relation between the jitter/deflection-angle signal and the wavefront. Therefore, (4.4) shows that the measured optical quantity, the jitter/deflection-angle spectrum, should in effect be *band-pass filtered* in order to calculate the level of aero-optical aberrations, $OPD_{r.m.s.}$, for a given aperture size.

From the cumulative function, $CG(t)$, see Figure 8b, it is clear that 95% of the “filtered energy” is located between $St_{Ap} = 0.28$ and 20. Therefore, the exact shape of the low-pass

filter (or more accurately, the fit) which is applied to the measured deflection angles to compensate for vibration contamination is essentially *irrelevant* below $St_{Ap} = 0.28$ (and above $St_{Ap} = 20$) as long as all non-physical components, like vibrations, are removed or suppressed by the empirical low-pass filter. Direct numerical calculations confirm these results. The selection of the high-pass filter is discussed later in this paper.

Although the transfer function (4.3) tends to suppress the electronic noise which shows up as spikes in the high end of the spectra, notch filters were applied to remove these spikes.

Before leaving this discussion of the aperture filter, it should be pointed out that the filter gain shown in Figure 8a, gives the effect of removing tip/tilt from the data for aberration spatial scales less than the aperture size; $[1 - G(Ap, f)]$ can be thought of as a low-pass filter for all of the beam tip/tilt that can be measured for a beam of a given aperture. This is an important recognition and will be used later to explain some of the variation in spectra for data taken at different facilities based now on the aperture of the small-beam, Malley probe.

4.2.3. *Relationship between $OPD_{r.m.s.}$ for propagation through SBL and DBL*

The next issue is dealing with the fact that the Malley probe beams pass through two independent boundary layers. Under the assumption that the two boundary layers are statistically independent, the resulting ‘optical energy’, $OPD_{r.m.s.}^2$, is a sum of the individual ‘optical energies’ from each boundary layer. Therefore, the optical aberration from the single boundary layer can be estimated from the double boundary layer measurements as,

$$OPD_{r.m.s.}^{SBL} = \frac{1}{\sqrt{2}} OPD_{r.m.s.}^{DBL}. \quad (4.5)$$

As will be shown later, this approach was fully vindicated by comparing the double boundary layer results with the single boundary layer results.

The resulting $OPD_{r.m.s.}$ from these and other data series at both Notre Dame and the United States Air Force Academy are calculated for both DBL and SBL; however, before discussing these results, it is helpful to formulate a theoretical framework in which to interpret the results.

4.2.4. *Models of optical distortions*

Statistical model

If the r.m.s.-distribution of the density, $\rho_{r.m.s.}(y)$, and the correlation lengths, $\Lambda_\rho(y)$, in the wall-normal direction are known, $OPD_{r.m.s.}$ can be calculated using the linking equation (1.3). From the equation of state it follows that the density fluctuations are functions of both pressure and static temperature fluctuations, $\rho'/\rho_\infty = p'/p_\infty - T'/T_\infty$. If the pressure fluctuations are assumed to be negligible inside the boundary layer, all density fluctuations are due to static temperature fluctuations, $\rho_{r.m.s.}/\rho_\infty = -T_{r.m.s.}/T_\infty$. Using Strong Reynolds Analogy (Morkivin 1962), $C_p T + u^2/2 = const$, temperature fluctuations are linked to velocity fluctuations as, $T_{r.m.s.}/T_\infty = -(\gamma - 1)u_{r.m.s.}Ua_\infty^{-2}$, where U is the mean velocity profile and finally, the density fluctuation profile can be calculated from the velocity profile, $\rho_{r.m.s.}(y)/\rho_\infty = (\gamma - 1)M_\infty^2 u_{r.m.s.}(y)U(y)U_\infty^{-2}$.

Using the velocity profile at $x = 156$ cm, see Figure 6a, the term $u_{r.m.s.}(y)U(y)U_\infty^{-2}$ is plotted in Figure 9a. Although the velocity fluctuations reach the maximum near the wall, the overall density fluctuations are small inside the log-region of the boundary layer, $y/\delta^* < 0.71$, thus placing the optically aberrating region, where ρ' is the largest, inside the outer region of the boundary layer.

Substituting this relation into the linking equation (1.3), the level of optical aberrations

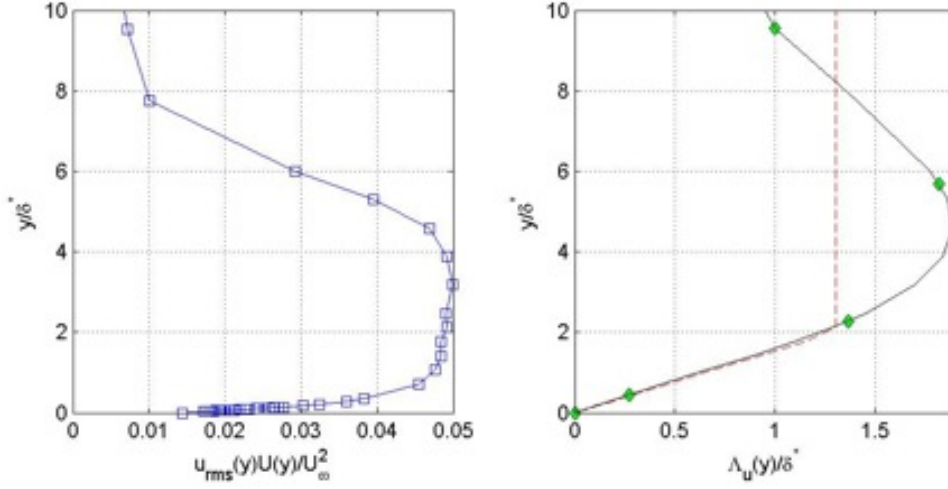


FIGURE 9. a) The term $u_{\text{r.m.s.}}(y)U(y)U_\infty^{-2}$. b) Cross-stream velocity correlation lengths, $\Lambda_u(y)$, from Buckner, Gordeyev & Jumper (2005) (dashed line) and from Gilbert (1982) (solid diamonds).

can be found as,

$$\text{OPD}_{\text{r.m.s.}} = A\delta^* \frac{\rho}{\rho_{\text{SL}}} M^2, \quad (4.6)$$

where $A = 2^{1/2}(\gamma - 1)K_{\text{GD}}\rho_{\text{SL}} \left\{ \int_0^\infty \left[\frac{u_{\text{r.m.s.}}(y)}{U_\infty} \frac{U(y)}{U_\infty} \right]^2 \frac{\Lambda_\rho(y)}{\delta^*} d(y/\delta^*) \right\}^{1/2}$ and ρ_{SL} is a reference sea-level density ($\rho_{\text{SL}} = 1.225 \text{ kg m}^{-3}$).

The statistically-based model (4.6) predicts that the optical aberration will be proportional to the freestream density, the boundary layer displacement thickness and a square of the freestream Mach number.

As density fluctuations are now assumed to depend on the velocity statistics only, it is reasonable to propose that density correlation lengths will be similar to the velocity wall-normal correlation lengths, $\Lambda_\rho(y) = \Lambda_u(y)$. Buckner *et al.* (2005) reported the wall-normal velocity correlation length to be approximately constant in the outer portion of the boundary layer, $\Lambda_u(y)/\delta^* = 1.33$, see Figure 9b. Gilbert (1982) reported experimentally measured velocity correlation lengths as a function of the wall-normal distance, also shown in Figure 9b. Overall, these results are consistent with previously reported

results (e.g. Grant 1958). Using velocity profiles given in Figure 6a the constant of proportionality in (4.6) was found to be $A = 2.0 \cdot 10^{-5}$ using velocity correlation lengths from Buckner *et al.* (2005) and $A = 2.1 \cdot 10^{-5}$ using Gilberts velocity correlation results (Gilbert 1982), so the constant is found to be relatively insensitive to the exact profile of the velocity correlation distribution.

The convective speed of the optical aberration can be estimated using the density distribution as a weighting function, $U_c = \int_0^\infty U(y)\rho_{r.m.s.}(y)dy / \int_0^\infty \rho_{r.m.s.}(y)dy$. Using the profiles from Figure 6a gives the value of the convective speed to be 0.85 of the freestream velocity, which is very close to the experimentally measured convective speed of 0.81 of the freestream speed.

Vortical-structure-based model

The statistical model, presented in the previous section fails to recognize the presence of the coherent vortical structures in the boundary layer. Also, it assumes the pressure fluctuations in the boundary layer to be negligible, which, as will be shown in Section 5, is not quite correct. So, a simple model for optical aberrations in a turbulent boundary layer at subsonic speeds, based on the assumption that large-scale vortices are present in the outer portion of the boundary layer, was developed. If these vortices are present, then in the same way that the coherent vortical structures in a free shear layer lead to low-pressure regions in the layer (Jumper & Fitzgerald 2001), a simple theory was developed to estimate the required pressure gradients that must be present to counter the centrifugal forces created by the curvature of the flow present in the vortices. Under this assumption, the pressure field is not constant inside of the vortical structure; these fluctuating pressure fields, in turn, create non-uniform density, and thus unsteady index-of-refraction distributions.

Consider a free, two-dimensional vortex with a Gaussian vorticity distribution, $\omega(r) \sim$

$\exp[-A(r/a)^2]$, where a denotes the core size and the constant A will be determined later. The azimuthal velocity profile can be found as,

$$u_\theta(r) = \frac{\int_0^r \omega(r')r'dr'}{r} \sim \frac{1 - \exp[-A(r/a)^2]}{r} = u_\theta^{\max} \frac{1 - \exp[-A(r/a)^2]}{B(r/a)}, \quad (4.7)$$

where u_θ^{\max} is the maximum azimuthal velocity reached at $r = a$. From this constraint, constants A and B can be estimated as $A = z = 1.256$ and $B = 1 - \exp(-A) = 0.715$, where z is a solution of the equation $2z + 1 = \exp(z)$.

For a two-dimensional, axisymmetric vortex, the Euler equations are reduced to a single equation for a pressure distribution across the vortex,

$$-\frac{u_\theta^2(r)}{r} = -\frac{1}{\rho} \frac{\partial p(r)}{\partial r} \approx -\frac{\gamma p_\infty}{\rho_\infty^2} \frac{\partial \rho(r)}{\partial r} = -\frac{\gamma RT_\infty}{\rho_\infty} \frac{\partial \rho(r)}{\partial r}, \quad (4.8)$$

where an isentropic relation between the density and the pressure is assumed, $p/p_\infty = (\rho/\rho_\infty)^\gamma$, as was done by Fitzgerald & Jumper (2004). So, the solution for the density distribution inside the vortex for small density fluctuations $\Delta\rho/\rho_\infty \ll 1$ can be found by substituting (4.7) into (4.8) and integrating. Finally, knowing the density variations as a function of space, the OPL can then be calculated directly by integrating the index of refraction along the propagation path using (1.2). For propagation directly through the centerline of the vortex, i.e., integrating the density distribution along r from $-\infty$ to $+\infty$, the OPL is,

$$\text{OPL}_{\text{vortex}} = \text{OPL}_{\text{free-space}} - 3.57(u_\theta^{\max}/a_\infty)^2 K_{\text{GD}} \rho_\infty a, \quad (4.9)$$

where $a_\infty = (\gamma RT_\infty)^{1/2}$ is the freestream speed of sound. Thus, the peak-to-peak OPD_{P-P} induced by the vortex is,

$$\text{OPL}_{\text{P-P}} = 3.57(u_\theta^{\max}/a_\infty)^2 K_{\text{GD}} \rho_\infty a. \quad (4.10)$$

Now consider a continuous line of vortices moving with a constant speed. Each vortex would distort a stationary beam and produce a time-varying OPD with a peak-to-peak

value given by (4.10). If these disturbances produce a near sinusoidal aberration, then $\text{OPD}_{\text{r.m.s.}} \approx (1/2\sqrt{2})\text{OPD}_{\text{P-P}}$. This gives a relationship for optical distortions as a function of freestream density, ρ_∞ , freestream velocity, U_∞ , vortex intensity, u_θ^{max} , and vortex size, a ,

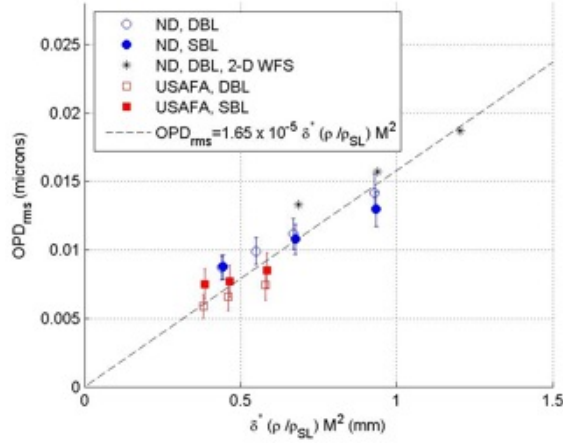
$$\text{OPD}_{\text{r.m.s.}} \approx \frac{3.57}{2\sqrt{2}} K_{\text{GD}} (u_\theta^{\text{max}}/a_\infty)^2 \rho_\infty a = 10.1 \cdot K_{\text{GD}} t^2 M_\infty^2 \rho_\infty a, \quad (4.11)$$

where $M_\infty = U_\infty/a_\infty$ and $t = 1/(2\sqrt{2})u_\theta^{\text{max}}$ can be treated as a relative r.m.s. turbulence intensity. Any intermittence in the train of convecting vortices would reduce the coefficient in (4.11), so that the estimate of the coefficient would, presumably, represent an upper bound.

Proposing that the optical structures reside in the outer part of the boundary layer, making the typical vortical sizes proportional to the boundary layer displacement thickness, $a \sim \delta^*$, the optical distortions from the subsonic boundary layers should scale as $\text{OPD}_{\text{r.m.s.}} \sim \delta^* \rho M^2$. So, both the statistical model (4.6) and the structural model (4.11) give the same scaling for subsonic turbulent boundary layers. Also notice that both models (4.6) and (4.11) give a linear dependence of the optical aberration versus the dynamic pressure, $q = 1/2\rho U^2$, consistent with Roses boundary layer scaling (Rose 1979) and the free shear layer weakly-compressible model (Fitzgerald & Jumper 2004), but not consistent with Gilbert (1982), who suggested a square root of dynamic pressure dependence.

4.2.5. *Optical distortion of vortical structures*

Using these scaling arguments, the optical distortions from the subsonic boundary layers should scale as $\text{OPD}_{\text{r.m.s.}} \sim \delta^*(\rho_o/\rho_{\text{SL}})M^2$. The $\text{OPD}_{\text{r.m.s.}}$ were calculated as described in Section 2 for an aperture size of $\text{Ap} = 0.25$ m and the results for both tests are shown in Figure 10, plotted against the scaling factor, $\delta^*(\rho/\rho_{\text{SL}})M^2$. Also shown in Figure

FIGURE 10. Boundary layer $OPD_{r.m.s.}$ scaling.

10 are data from the Notre Dame tunnel made with a conventional wavefront sensor demonstrating that the Malley-Probe one-dimensional wavefront data are consistent with two-dimensional wavefront data made in the same facility. The experimental data does indeed follow the proposed scaling, with a linear fit through the data, also shown in Figure 10, as

$$OPD_{r.m.s.} = (1.65 \pm 0.30) \cdot 10^{-5} \delta^2 \frac{\rho}{\rho_{SL}} M^2, \quad (4.12)$$

Figure 10 shows that both ND single and double boundary layer experiments recover the correct average level of optical aberrations, confirming (4.5). Amplitudes of $OPD_{r.m.s.}$ from USAFA single boundary layer experiment were slightly higher than $OPD_{r.m.s.}$ from the double boundary layer experiment. Inspection of the raw data revealed some degree of the signal contamination due to an optical imperfection of the optical insert for USAFA experiments, perhaps explaining the slight increase seen in the optical distortion from the Academy data.

Gilbert (1982) presented one of the first direct (fast-shearing interferometry) and indirect hotwire measurements of the optical distortions caused a subsonic turbulent boundary layer using the linking equation (1.3) and extracting the density fluctuations, pre-

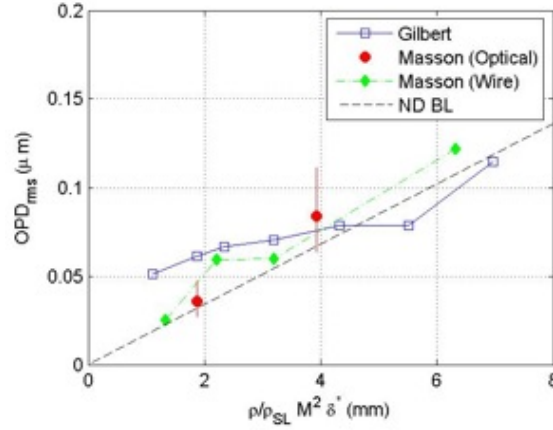


FIGURE 11. Comparison between different boundary layer experiments.

suming the pressure fluctuations were negligible. Gilbert’s measurements were taken at Mach numbers ranging from 0.25 to 0.85 for different altitudes between 0.3 and 11.3 km. Boundary layer displacement thicknesses, δ^* , were estimated from velocity profiles measured by Rose, Johnson & Otten (1982) during the same experiments and found to be approximately 22 mm. Gilbert’s results are presented in Figure 11 along with Notre Dame boundary layer scaling (4.12), plotted as a dashed line for comparison. Data agree quite well at high “ ρM^2 ”, but at low “ ρM^2 ” Gilbert’s data are consistently higher than (4.12) predicts. Masson *et al.* (1994) revisited some of the Gilbert’s data and found systematic error in reducing that data, which lead to overestimating optical distortions at low Mach numbers. After correction, Masson’s data points, also plotted in Figure 11 for both from direct (optical) and indirect (hotwire-based) measurements, agree much better with (4.12).

Spectral scaling

From (2.2) and (4.12) it follows that the deflection-angle data scales as,

$$\theta(t) \propto \frac{\delta^*(\rho/\rho_{SL})M^2 f_{\text{samp}}}{U_\infty}, \quad (4.13)$$

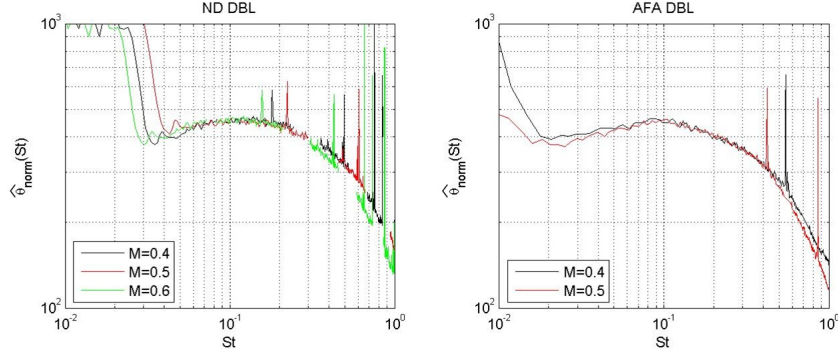


FIGURE 12. The normalized jitter spectra for a) ND and b) USAFA double boundary layer experiments for several Mach numbers.

where f_{samp} is the sampling frequency and $U_c \sim U_\infty$. Similarly, the deflection angle amplitude spectrum scales as, $\hat{\theta}(f) = \int \theta(t) \exp(-i\omega t) dt \propto \delta^*(\rho/\rho_{\text{SL}}) M^2 / U_\infty$. Thus, boundary layer jitter amplitude spectrum can be presented as,

$$\hat{\theta}(f) = \frac{\rho}{\rho_{\text{SL}}} M^2 \frac{\delta^*}{U_\infty} \hat{\theta}_{\text{norm}} \left(\frac{f \delta^*}{U_\infty} \right). \quad (4.14)$$

where throughout the rest of the paper, $St = f \delta^* / U_\infty$, is the Strouhal number based on the local displacement thickness, δ^* , unless noted otherwise. The normalized jitter amplitude spectra, $\hat{\theta}_{\text{norm}}(St)$, from boundary layer experiments at several Mach numbers and two facilities are plotted in Figure 12. The ND spectra collapse onto one curve between $St = 0.04$ and 0.4 and the USAFA spectra collapse between 0.01 and 0.4 , showing that for these data the scaling in (4.14) appears to be correct. Deviation below $St = 0.04$ is due to the mechanical-vibration contamination. The collapsed shapes are slightly different for each experiment and a possible reason for these differences is offered in the following section.

Both normalized amplitude spectra exhibit a single peak at $St \sim 0.1$. The location of the boundary layer “hump” is also in agreement with the earlier findings of Wittich *et al.* (2007). It was already pointed out that if the Strouhal number of the abscissa is written in terms of the boundary layer thickness, δ , instead of the displacement thickness,

the ‘peak’ of the boundary layer spectrum occurs near $St_\delta \sim 1$, again pointing to the large-scale nature of the optical aberrations.

Finite Malley probe beam-size effects

While the deflection spectra show a good collapse below $St = 0.4$, above it the spectra start deviating from each other; furthermore, the USAFA spectrum start deviating from ND spectrum at even smaller $St = 0.1$. The corresponding streamwise size or wavelength, Λ , of the pure convecting optical structure is,

$$\Lambda = U_c/f = \delta^* \frac{U_c}{U_\infty} \frac{U_\infty}{f\delta^*} = 0.81 \frac{\delta^*}{St}, \quad (4.15)$$

which is approximately $\Lambda = 2\delta^*$ for $St = 0.4$ or approximately 7 mm for the ND experiment. The Malley probe beams were about 1 mm in diameter for ND experiments and about 2 mm for USAFA experiments. As noted at the end of the previous section, the finite beam size/aperture modifies the measured deflection angle, when the structures are on the order or less than the beam size (Siegenthaler *et al.* 2005; Siegenthaler 2008),

$$\hat{\theta}_{\text{measured}}(\Lambda)/\hat{\theta}_{\text{true}}(\Lambda) = G(\Lambda). \quad (4.16)$$

For the sensor used to measure the deflection angle in these experiments, the transfer function was shown to be a low-pass transfer function $G(\Lambda) = \text{sinc}(A_{\text{SB}}/\Lambda)$, where A_{SB} is the small-aperture laser-beam size (Siegenthaler 2008). For $\Lambda/A_{\text{SB}} = 1.67$, $G(A_{\text{SB}}/\Lambda) = 0.5$ or -3 dB and for $\Lambda = 7$ mm and $A_{\text{SB}} = 1$ mm, $G(A_{\text{SB}}/\Lambda) = 0.97$. To reconstruct the *true* deflection angle spectrum, the *measured* deflection spectrum should be corrected for ‘finite-beam-size’ effects using (4.16) and the frozen field hypothesis, linking the wavelength to the frequency (4.15). The corrected normalized spectra are shown in Figure 13; the corrected data collapse well up to $St = 1$. The empirical curve-fit through all data, shown as a dashed line in Figure 13, is,

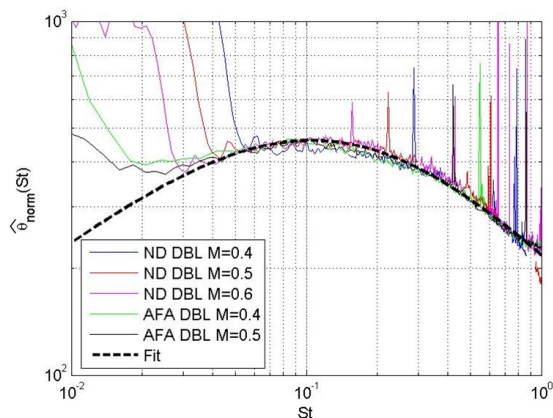


FIGURE 13. The normalized jitter spectra for ND and USAFA double boundary layer experiments for several Mach numbers, corrected for a finite beam size.

$$\hat{\theta}_{\text{norm}}(St) \sim \frac{St^{1/2}}{1 + (St/0.135)^{7/6}}. \quad (4.17)$$

The deflection spectrum (4.17) behaves as $\hat{\theta}(St) \sim St^{-2/3}$ for large frequencies. Later in Section 4.2.7 this curve-fit can be used to estimate the streamwise correlation lengths. It should also be pointed out that this correction to the higher-frequency portion of the spectrum has little effect on the estimate of $\text{OPD}_{\text{r.m.s.}}$ due, again, to the discussion in the previous section.

Spectrum behaviour at high frequencies

Tatarski (1961) showed that if the cause of the optical aberrations is the fluctuation of a passive scalar like total temperature, which is the main mechanism of the atmospheric optical aberrations, the spectral density of the *two-dimensional* wavefront passing through the media is $\Phi(k) \sim k^{-11/3}$ for large wave numbers. But Tatarski also showed that if the optical aberrations are due to pressure fluctuations, $p \sim \rho u'^2$, the spectral density of the 2-D wavefront behaves as $\Phi(k) \sim k^{-13/3}$ for large wave numbers.

The Malley probe measures *one-dimensional* wavefronts, $\text{OPD}(x)$, with a corresponding spectral density, $S_{\text{OPD}}(k) \sim |A_{\text{OPD}}(k)|^2$, where $A_{\text{OPD}}(k)$ is the Fourier transform of

OPD(x). The relation between the 2-D and 1-D wavefront spectral densities is $\Phi(k)d\vec{k} \sim \Phi(k)kdk \sim S_W(k)dk$, so $\Phi(k)k \sim |A_{\text{OPD}}(k)|^2$. From (2.2), the deflection angle spectrum is $\hat{\theta}(f) \sim f \cdot A_{\text{OPD}}(f)$. Finally, recognizing that the optical structures travel with a speed, U_c , so $f = kU_c/(2\pi)$, the deflection angle spectrum measured by the Malley probe is related to the 2-D wavefront spectral density as $\hat{\theta}(f) \sim f [\Phi(f)f]^{1/2} = f^{3/2}\Phi(f)^{1/2}$. So if pressure fluctuations are the cause of the optical distortions in the turbulent boundary layer, $\Phi(f) \sim f^{-13/3}$ and $\hat{\theta}(f) \sim f^{3/2}f^{-13/6} = f^{-2/3}$, which is consistent with the experimentally observed behavior of the deflection angle spectrum (4.17). Thus, the physical mechanism of the optical aberrations in the boundary layer are quite different from the atmosphere-related optical aberrations, for which $\Phi(f) \sim f^{-11/3}$ and the deflection angle amplitude spectrum should behave as $\hat{\theta}(f) \sim f^{3/2}f^{-11/6} = f^{-1/3}$.

Since static temperature fluctuations are also proportional to the velocity squared, $T' \sim u^2$, they would manifest themselves as $\hat{\theta}(f) \sim f^{-2/3}$ in the deflection-angle spectra, similar to the pressure-based optical distortions. Thus, the analysis of the high-frequency portion of the deflection-angle spectra cannot answer whether optical distortions are due to the static temperature variations (the statistical model (4.6)), pressure fluctuations inside the vortical structures (the vortical model (4.11)) or a combination of both effects.

4.2.6. *Oblique elevation angles*

It might be presumed that it would be possible to extend the deflection-angle-spectrum scaling described in the previous section for arbitrary elevation angles, β . When the laser beam travels through the boundary layer at an oblique angle, it traverses a longer distance $\delta^*/\sin(\beta)$ inside the boundary layer, see Figure 14. A simple presumed correction to account for oblique propagation on $\text{OPD}_{\text{r.m.s.}}$ would be to replace δ^* with $\delta^*/\sin(\beta)$ in equation (4.12);

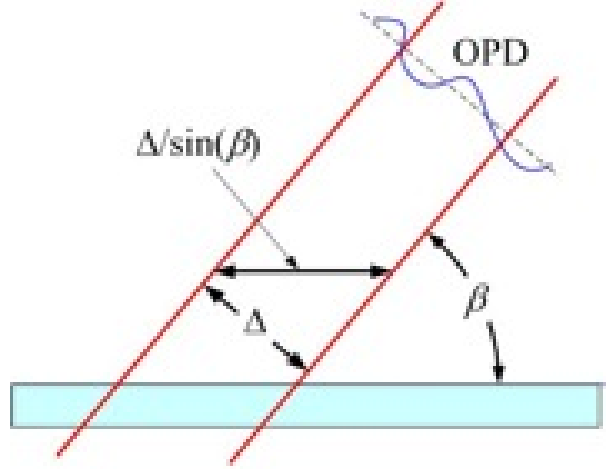


FIGURE 14. Malley probe calculation of OPD for an oblique elevation angle.

$$\text{OPD}_{\text{r.m.s.}} \sim \frac{\delta^*}{\sin(\beta)} \frac{\rho}{\rho_{\text{SL}}} M^2. \quad (4.18)$$

As before, the wavefront, or OPD, is calculated from the deflection angle, $\theta(t)$, using the convective speed, (2.2); however, as the diagram in Figure 14 shows, the convective speed *in the direction normal to the laser beams* is $U_n = \Delta/\tau^{\text{delay}}$, where τ^{delay} is the correlation time delay between the upstream and downstream beams. The Malley probe measures U_n , which must not be confused with the total convective speed, U_c , which is $U_c = \Delta/[\tau^{\text{delay}} \sin(\beta)] = U_n/\sin(\beta)$. Therefore, equation (2.2) for an arbitrary oblique propagation angle should be written as,

$$\text{OPD} \sim U_n \int \theta(t) dt = U_c \sin(\beta) \int \theta(t) dt. \quad (4.19)$$

Combining equations (4.18) and (4.19) gives the presumed scaling for an oblique propagation angle, β , spectrum as,

$$\hat{\theta}(f) = \frac{\rho}{\rho_{\text{SL}}} M^2 \frac{\delta^*}{U_\infty} \frac{1}{\sin^2(\beta)} \hat{\theta}_{\text{norm}} \left(\frac{St}{\sin(\beta)} \right). \quad (4.20)$$

Deflection angle amplitude spectra from single boundary layer measurements at the USAFA tunnel for $M = 0.5$ were scaled using the presumed angular dependence (4.20), and the results are shown in Figure 15a. The single boundary layer “angle-corrected”

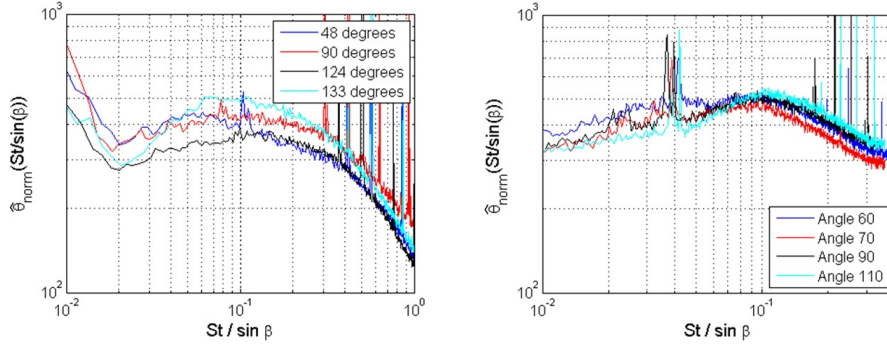


FIGURE 15. a) USAFA single boundary layer normalized jitter spectra with angular dependence as a function of $St/\sin(\beta)$ for Mach 0.5 and 4 elevation angles, b) Notre Dame single boundary layer normalized jitter spectra with angular dependence as a function of $St/\sin(\beta)$ for $M = 0.6$ and 4 elevation angles.

data using (4.20) did appear to draw these and all other Mach number data (not shown) closer; however there were still small, but noticeable differences between different oblique angles. For instance, focusing on “angle-corrected” results for the upstream oblique angle of 48° and the symmetric (about the vertical axis) downstream oblique angle of 133° , according to the simple angular dependence scaling argument (4.20), these spectra should be identical, since $\sin(48^\circ) \approx \sin(133^\circ)$; instead, as Figure 15a shows, the 133° case is consistently higher than the 48° case in the range of normalized frequencies $St/\sin(\beta) = 0.06..0.5$.

It is well-established that the turbulent boundary layer has packets of vortical structures with a preferred angular direction (Adrian 2007; Adrian, Meinhart & Tomkins 2000; Hutchins, Hambleton & Marisic 2005; Robinson 1991), see Figure 16; thus, it should exhibit an anisotropic behavior for different oblique angles. Anisotropy of optical aberrations was also observed in numerical simulations of Truman & Lee (1990), albeit that the aberrations were due to temperature fluctuations carried as a passive scalar. If this conventional wisdom regarding directional anisotropy is correct, a consequence should be that in the downstream-direction propagation through elongated structures should result

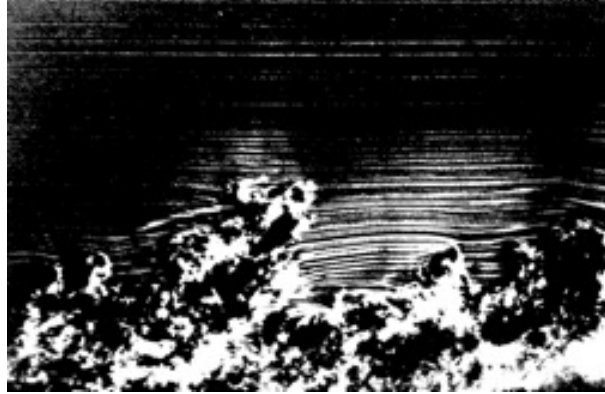


FIGURE 16. Elongated vortical structures in the turbulent boundary layer; flow goes from left to right. (van Dyke 1982).

in more aberration, versus propagation in the upstream direction. Thus, the differences in observed deflection-angle spectra in the oblique propagation data provide additional comparative evidence for the preferred angular orientation of boundary-layer structures. As seen in Figure 15a, this holds true except for the 124° case, where the deflection angle spectrum drops below all other spectra, which may or may not be significant.

Scaled results of single boundary layer measurements taken at Notre Dame are shown in Figure 15b. Narrow peaks around $St/\sin(\beta) = 0.04$ are due to tunnel-induced vibrations. For a fixed oblique-propagation angle, results collapse for all Mach numbers tested (not shown in Figure 15b for clarity), but the normalized data also exhibit the same anisotropic behavior with the 110° case showing an anomaly similar to the 124° case from the USAFA; again this may or may not be significant.

From the deflection-angle temporal data, one-dimensional wavefront slices were calculated, as discussed in Section 2. The wavefront results were apertured to 0.25 m and, $OPD_{r.m.s.}$, was calculated for all cases.

The wavefront results for the USAFA double boundary layer tests are plotted in Figure 17 versus the oblique-propagation-angle dependence, equation (4.18). Since in these tests

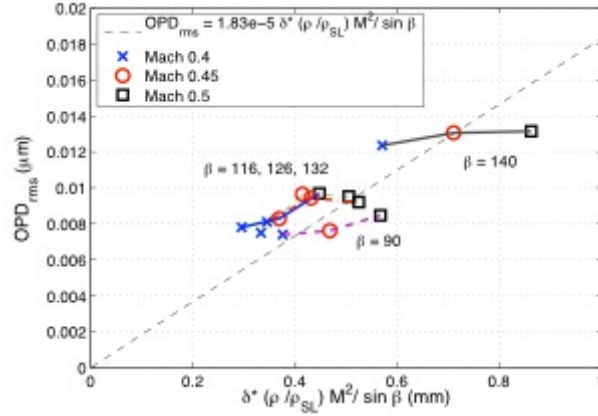


FIGURE 17. USAFA double boundary layer $OPD_{r.m.s.}$ scaling. Three Mach numbers and five elevation angles are shown.

the laser beam traversed through two boundary layers, the levels of optical aberrations for a single boundary layer were estimated from $OPD_{r.m.s.}$ for double boundary layers using equation (4.5). The results collapse reasonably well onto a single line for all Mach numbers and elevation angles, leading one to infer that the angular dependence is essentially cancelled by propagation downstream on one boundary layer and upstream on the second boundary layer. The least-square analysis gives the best linear fit (shown as a dotted line) with a constant slope of $1.83 \cdot 10^{-5}$. This value is close to the value of $1.65 \cdot 10^{-5}$, found for the normal elevation angle measurement (4.12).

Wavefront results for the USAFA single boundary layer tests are shown in Figure 18. The 48° and 90° cases collapse onto a single line. However, the look back elevation angles are slightly higher than the forward-looking angles; these results are consistent with an anisotropic behavior of the boundary layer, discussed earlier. An overall slope marked by a dashed line in Figure 18 was found to be approximately $1.6 \cdot 10^{-5}$.

Wavefront results for Notre Dame single boundary layer are plotted in Figure 19. They also collapse onto a single line, although the proportionally constant in (4.18) was found

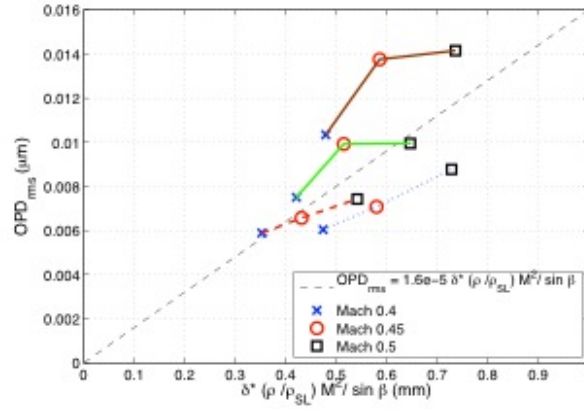


FIGURE 18. USAFA single boundary layer $OPD_{r.m.s.}$ scaling. Three Mach numbers and four elevation angles are shown.

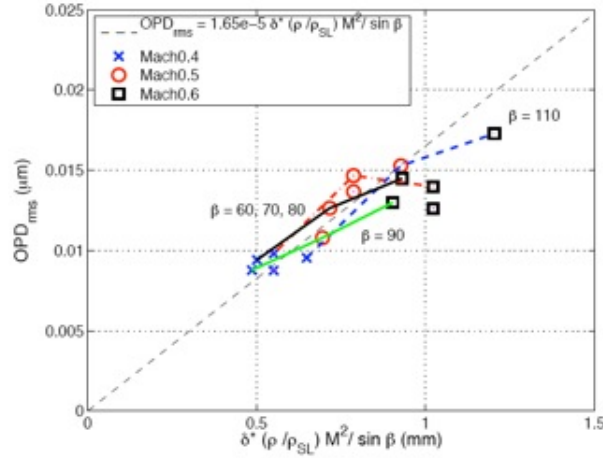


FIGURE 19. Notre Dame single boundary layer $OPD_{r.m.s.}$ scaling. Three Mach numbers and five elevation angles are shown.

to be $1.65 \cdot 10^{-5}$. All of these linear-fit-slope values are within the range of uncertainty of the data.

Combining results of optical distortions caused by turbulent boundary layers from the USAFA and ND tests including oblique-propagation effects yields the following scaling law,

$$OPD_{r.m.s.} = (1.7 \pm 0.2) \cdot 10^{-5} \frac{\delta^*}{\sin(\beta)} \frac{\rho}{\rho_{SL}} M^2. \quad (4.21)$$

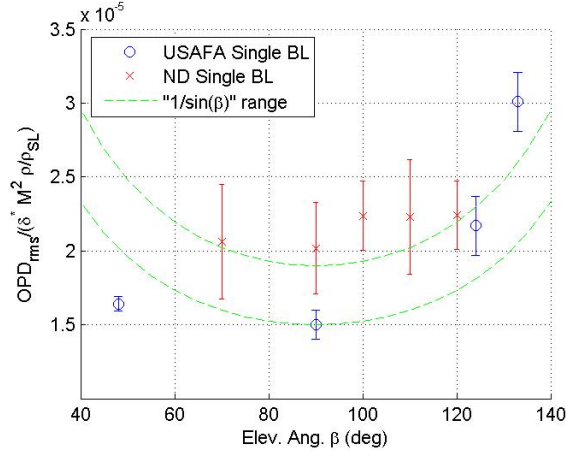


FIGURE 20. Single boundary layer $OPD_{r.m.s.}$ data versus the elevation angle.

Note that this simple empirical relation does not include anisotropic behavior of optically-aberrating structures in the turbulent boundary layer. The anisotropic behavior is best seen by combining the results from all the data normalized only by $\delta^* \rho / \rho_{SL} M^2$ against oblique angle; this has been done in Figure 20. The “isotropic” oblique-propagation angular dependence from equation (4.21), “ $1/\sin(\beta)$ ”, is also plotted in Figure 20. While the “isotropic” curve-fit does a decent job for elevation angles between 70° and 120° , it overestimates optical aberrations at forward-looking angles below 50° and underestimates optical distortion above 130° .

4.2.7. Optical cross-correlation results

Spanwise correlation length

The spanwise, or transverse, correlation length was measured in other experiments using the two Malley probes at the same streamwise, x , location but varied in the spanwise, z , direction, see Figure 21. Time series of deflection angles at each location were measured and the OPD values were reconstructed. The OPD cross-correlation coefficients were computed as,

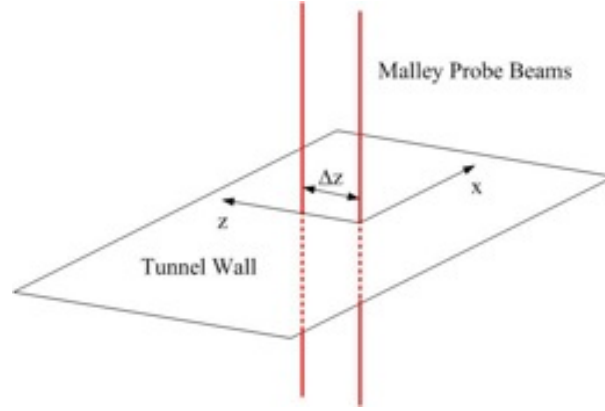


FIGURE 21. Spanwise correlation set-up.

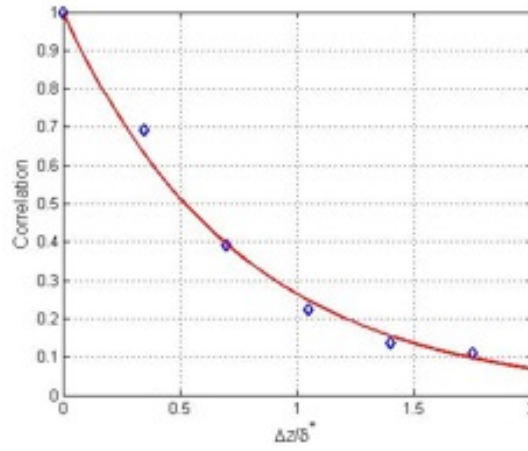


FIGURE 22. Optical spanwise correlation decays exponentially with spanwise separation. The spanwise correlation length, Λ_z , defined by (4.22), is approximately $0.75\delta^*$.

$$\rho_z(\Delta z) = \frac{\overline{\text{OPD}(z, t)\text{OPD}(z + \Delta z, t)}}{\overline{\text{OPD}(z, t)^2}}, \quad (4.22)$$

The correlations are shown in Figure 22 along with an exponential curve-fit,

$$\rho_z(\Delta z) = \exp\left(-\frac{|\Delta z|}{\Lambda_z}\right). \quad (4.23)$$

The exponential fit of the data gives a spanwise correlation length, $\Lambda_z \approx 0.75\delta^*$

Streamwise correlation function

A time-delayed auto-correlation function, $R_{\text{OPD}}(\tau)$ is defined as,

$$R_{\text{OPD}}(\tau) = \overline{\text{OPD}(t)\text{OPD}(t + \tau)}, \quad (4.24)$$

where the overbar denotes the temporal averaging. The auto-correlation function, $R_{\text{OPD}}(\tau)$, can be calculated from the spectral auto-correlation function, $S_{\text{OPD}}(f)$ as,

$$R_{\text{OPD}}(\tau) = \int S_{\text{OPD}}(f)\exp(2\pi i f \tau)df = \int \frac{A_{\text{OPD}}(f)A_{\text{OPD}}^*(f)}{T}\exp(2\pi i f \tau)df, \quad (4.25)$$

where $A_{\text{OPD}}(f)$ is the Fourier transform of $\text{OPD}(t)$, T is the block duration, brackets denote an ensemble averaging and the asterisk denotes a complex conjugate. $A_{\text{OPD}}(f)$ can be found from the deflection-angle spectra, since from (2.2) it follows that $A_{\text{OPD}}(f) = -U_c \hat{\theta}(f)/[2\pi f]$ and (4.25) becomes,

$$R_{\text{OPD}}(\tau) = \frac{U_c^2}{4\pi^2 T} \int \frac{|\hat{\theta}(f)|^2}{f^2} \exp(2\pi i f \tau) df. \quad (4.26)$$

In order to compute the auto-correlation function, the normalized deflection-angle amplitude spectra, Figure 13, was approximated with an empirical curve fit (4.17), $\hat{\theta}_{\text{norm}}(St) \sim St^{1/2} [1 + (St/0.135)]^{-7/6}$. The amplitude spectrum behaves as $\hat{\theta}_{\text{norm}}(St) \sim St^{1/2}$ for small $St \ll 1$, so technically the integral (4.26) diverges. Physically it means that the very large scales (or small frequencies) are present in the empirical spectra; however experimentally, it was shown that the biggest scale of coherent structures present in turbulent boundary layers is on the order of ten boundary layer thicknesses or $\sim 80\delta^*$, so it is reasonable to filter out any structures above this size. After the filtering the integral (4.26) is well-defined and the normalized auto-correlation function, $\rho_x(\tau) = R_{\text{OPD}}(\tau)/R_{\text{OPD}}(0)$, can be calculated using (4.26). Different high-pass filters with a cut-off wavelength of $80\delta^*$, which, via (4.15), corresponds to the frequency cut-off St of 0.01, were applied to the empirical curve-fit. Using the frozen convection assumption, the time delay then was converted into the streamwise separation, $\Delta x = -U_c \tau$. The results for dif-

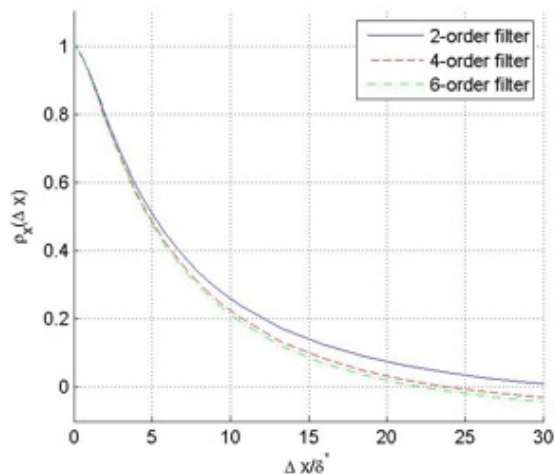


FIGURE 23. The boundary layer streamwise normalized auto-correlation for different high-pass filters with a cut-off $St = 0.01$.

ferent filters are plotted in Figure 23. Compared with the spanwise correlation function, Figure 22, the streamwise correlation lengths decay much slower and are non-zero up to $\Delta x/\delta^* \sim 20$. The integral streamwise length, computed as $\Lambda_x = \int_0^\infty \rho_x(\Delta x)d(\Delta x)$, was found to be $\Lambda_x/\delta^* = 5.9$, 5.3 and 5.1 for the 2nd-, 4th- and 6th-order high-pass filters, respectively. These lengths correlate well with optical correlation length of $4\delta^*$, reported in Malley *et al.* (1992) and $5.2\delta^*$ found in Wittich *et al.* (2007). All these findings indicate the presence of large-scale streamwise-elongated optically-aberrating structures in the outer part of the boundary layer with a typical spanwise scale of $\sim \delta^*$ and streamwise length of $\sim 5\delta^*$ convecting at approximately 0.8 of the freestream velocity.

4.2.8. Boundary layer wavefront simulations

Knowing the streamwise and spanwise spectral functions, one can construct uncorrelated series of 2-D boundary layer wavefront realizations, $W(x, z)$, which, on average, satisfy the observed boundary layer statistics, that is,

$$\overline{W(x, z)W(x + \Delta x, z)} = \rho(\Delta x),$$

$$\overline{W(x, z)W(x, z + \Delta z)} = \rho(\Delta z), \quad (4.27)$$

$$W_{\text{r.m.s.}} = \text{OPD}_{\text{r.m.s.}} = 1.7 \cdot 10^{-5} \frac{\rho}{\rho_{\text{SL}}} \delta^* M^2.$$

Without loss of generality, we constructed wavefront realizations which have a normalized deviation, $W_{\text{r.m.s.}} = 1$.

We constructed wavefronts as a collection of uncorrelated 2-D harmonics with random phases,

$$W(x, z) = \sum_n \frac{\int_{-\infty}^{\infty} \int_{-\infty}^{\infty} \sqrt{\lambda(k_x, k_z)} \sqrt{\frac{a_n^2 + b_n^2}{2}} \exp[i(k_x x + k_z z + \phi_n)] dk_x dk_z}{\sqrt{\int_{-\infty}^{\infty} \int_{-\infty}^{\infty} \lambda(k_x, k_z) dk_x dk_z}}, \quad (4.28)$$

where a_n and b_n are random, normally distributed coefficients with a zero mean and a unity standard deviation, $a_n, b_n \sim N(0, 1)$, ϕ_n is a uniformly distributed random phase and $\lambda(k_x, k_z)$ is the spectral energy of each harmonic. Further, we approximated the spectral energy as a product of streamwise and spanwise components, $\lambda(k_x, k_z) = \lambda_x(k_x)\lambda_z(k_z)$, where $\lambda_z(k_z) = \left| \int_{-\infty}^{\infty} \rho_z(\Delta z) \exp(-ik_z \Delta z) d(\Delta z) \right| = 2\Lambda_z / [1 + (\Lambda_z k_z)^2]^{-1}$ and $\lambda_x(k_x) = |A_{\text{OPD}}(k_x)|^2$ can be found from the deflection angle spectrum curve fit (4.17) with the applied high-pass filter and using the frozen field assumption, $k_x = 2\pi f / U_c = 2\pi f \delta^* / (0.81 \delta^* U_\infty) = 2\pi St / (0.81 \delta^*) = St / (0.13 \delta^*)$,

$$\lambda_x(k_x) = |A_{\text{OPD}}(k_x)|^2 \sim \frac{|\hat{\theta}_{\text{norm}}(k_x)|^2}{k_x^2}. \quad (4.29)$$

Two examples of wavefront realizations as contour surfaces are shown in Figure 24, left. As expected, they show the presence of large-scale, streamwise-elongated structures. For comparison, two experimentally-obtained, boundary layer 2-D wavefronts from the double boundary layer experiments at Notre Dame, are shown in Figure 24, right. Although showing combined optical aberrations from two independent boundary layers, these 2-D wavefronts also reveal the presence of streamwise-elongated optical structures.

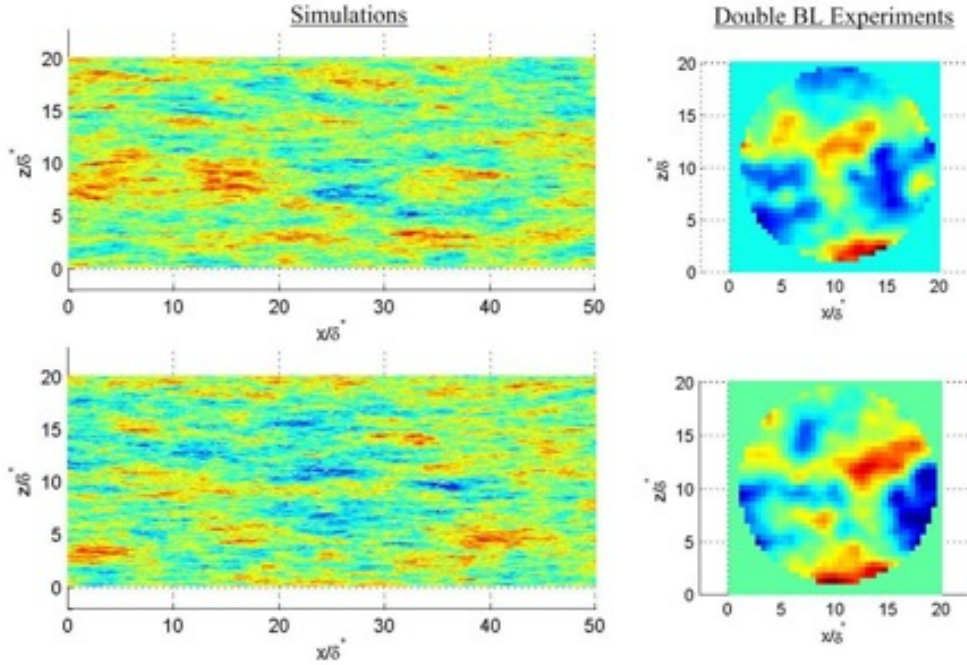


FIGURE 24. 2-D boundary layer wavefront realizations (4.28) (left column) and experimental 2-D wavefronts from ND double boundary layer experiments (right column).

These simulations provide statistically-correct realizations of the turbulent boundary layers and can be used, for instance, to simulate effects from realistic turbulent boundary layers if the boundary layer thickness, the freestream density and the incoming Mach numbers are provided. These simulations can be easily extended to include elevation angle effects.

Tomkins & Adrian (2003), among many other researchers (e.g. Adrian *et al.* 2000; Hutchins *et al.* 2005), have found elongated low-momentum vortical regions, “packets”, extending into the outer part of the boundary layer up to $y/\delta \sim 0.6$ with the streamwise length-scales of approximately $5 - 8\delta^*$ and spanwise length-scales between 0.5 and $1.3\delta^*$. Also, the speed of these large-scale structures was found to be approximately 0.8 of the freestream speed, and independent of Reynolds number (Adrian *et al.* 2000). These values agree well with optical correlation lengths and convective speed, reported here, suggesting

that the observed “packets” are responsible for or at least related to the observed optical aberrations.

4.2.9. Instantaneous far-field intensity drop-outs

As mentioned in the introduction, because the time-averaged Strehl ratios for beams transmitted through most attached turbulent boundary layers are usually quite high, turbulent boundary layers have always been presumed to be an aero-optic non-issue; however in Gordeyev *et al.* (2003) the issue of intermittent dropouts was raised. Additional research in recent years (e.g. Wittich *et al.* 2007) is yielding a more complete 2-D picture of the aberrating boundary-layer structures, and while the general comments regarding time-averaged Strehl ratio remain unchanged, the warnings of possible dropout problems now seem more likely to cause a serious deterioration of transmitted laser communication signals.

Because Malley probes actually measure time histories of $OPD(t)$, it is possible to construct a time series of $OPD(x, t)$ over the finite aperture by using the convective velocity. Thus, for a given aperture, the time-resolved Strehl ratio as a function of time can be computed. This was done for two aperture sizes, $Ap = 10$ and 50 cm; the experimentally measured OPDs were rescaled in amplitude for two boundary-layer thicknesses of $\delta = 10$ and 20 cm which represent distances of from $7 - 12$ m aft of the nose of the aircraft for $M = 0.8$, using (4.12). Results are plotted in Figure 25 for two communication laser wavelengths, $1.0 \mu\text{m}$ and $1.5 \mu\text{m}$. While the average intensity is still relatively high in all cases, it is clear that there are many dropouts, which last for several milliseconds, especially for larger apertures. Assuming a fast steering mirror, small apertures work as a natural high-pass filters reducing $OPD_{r.m.s.}$ (Siegenthaler *et al.* 2005; Siegenthaler 2008), therefore presenting less of a problem for far-field energy losses. From a laser-based communication point of view, these energy drop-outs might translate into a loss

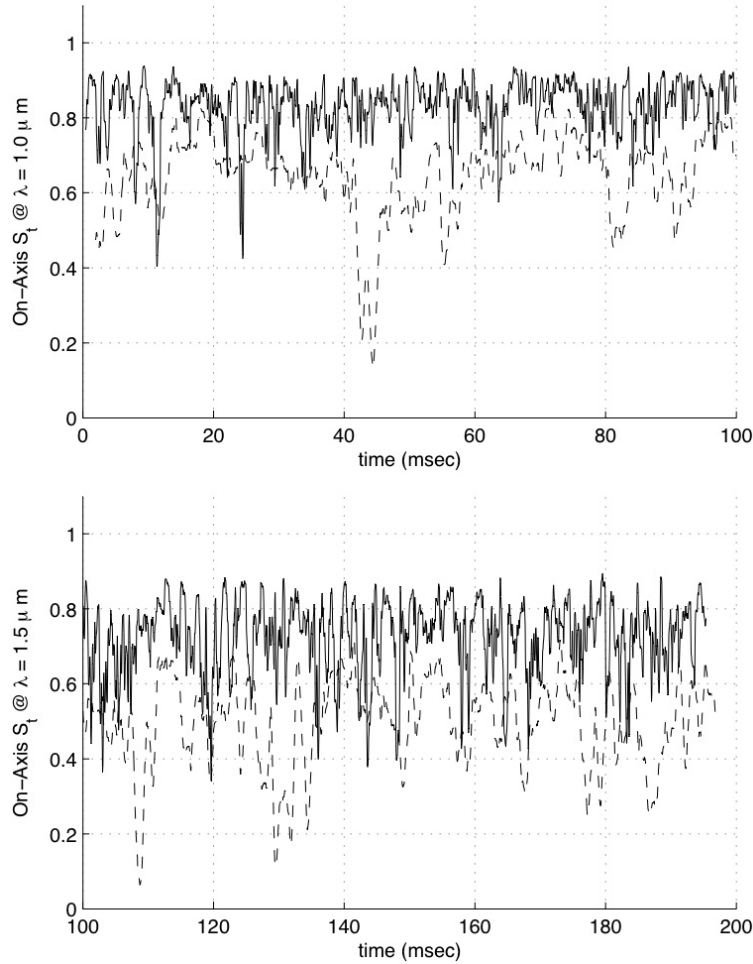


FIGURE 25. Instantaneous far-field Strehl ratios, S_t , as a function of time for laser beams propagated through boundary layers for different beam apertures, 0.1 m (solid line) and 0.5 m (dashed line) top) for a $\delta = 10$ cm and a $1.0 \mu\text{m}$ laser wavelength; bottom) for a $\delta = 20$ cm and a $1.5 \mu\text{m}$ laser wavelength. Tilt is removed, $M = 0.7$.

of several Gigabytes of data during each drop-out, inevitably slowing the communication link, since the lost chunks of data, must be constantly retransmitted. It should also be pointed out that these predictions are based on the beam being projected normal to the boundary layer; the OPD increases when the beam is projected through the boundary layer at oblique angles (4.18) thus making the intensity drop-out problem even worse.

5. Discussion and conclusions

Direct optical measurements of the optical aberrations caused by the compressible subsonic boundary layer with a zero-pressure gradient were measured experimentally as a function of the freestream Mach number, the boundary layer thickness and range of oblique-propagation angles, using a Malley probe and a two-dimensional wavefront sensor. Both a statistical model and a simple physical model based on pressure fluctuations inside the vortical structures in the outer region of the boundary layer were presented to help explain the level of optical distortions and provide a basis for scaling the data. All the data from different experimental facilities exhibit very-good collapse on the functional dependence derived from both models, $OPD_{r.m.s.} \sim \delta^* \sin^{-1}(\beta) \rho / \rho_{SL} M^2$. The average convective speed of the optical aberration was measured directly by the Malley probe and was found to be 0.81 of the freestream speed. The streamwise and the spanwise correlation lengths were measured to be approximately 5 and 0.75 of the displacement thickness, respectively. Significant far-field intensity drop-outs were observed, which, if left untreated, might seriously slow down data transmission rates of laser-based communication systems.

Some early studies of the optical properties of the boundary layers were based on the density measurements estimated from hotwire data and assuming that pressure fluctuations were negligible (e.g. Sutton 1985; Rose 1979), *t.e.* using the Strong Reynolds Analogy (Morkovin 1962), $T_{r.m.s.}/\bar{T} = (\gamma - 1)M^2 u_{r.m.s.}/\bar{U}$. Sutton (1985) proposed that the leading factors that contribute to the density variations causing optical aberrations inside the compressible subsonic boundary layers were: (i) pressure fluctuations, (ii) static temperature variations due to the Strong Reynolds Analogy mechanism, and (iii) the heat flux due to the small temperature difference between the flow total temperature and the wall “recovery” temperature, with the dominant mechanism being the Strong Reynolds

Analogy. Note that the pressure variations also lead to static temperature variations, but the physical *cause* of these temperature variations is *different* from the temperature variations due to velocity fluctuations.

Since pressure and static temperature fluctuations vary with the local speed as M^2 , both of these effects result in the experimentally observed “ $-2/3$ ” slope in the deflection angle spectra, see Figure 13 and the discussion at the end of Section 4.2.5; however, any addition of heat into the boundary layer due to a mismatch between the flow total temperature and the wall recovery temperature would introduce a passive temperature marker into the flow, which would result in a “ $-1/3$ ” slope in the deflection angle spectrum. Therefore, it is unlikely that the total temperature mismatch contributes significantly to the optical aberrations caused by subsonic turbulent boundary layers. But for the case of a heated wall or a supersonic boundary layer, this effect can become a significant contributor to the optical aberrations.

Pressure and static temperature are coupled through the equation of state, $p = \rho RT$, and it's hard to separate their individual contributions based on the density measurements alone. But the traditional assumption that the pressure fluctuations inside boundary layers are negligible has been convincingly shown not to be valid. The wall pressure beneath the boundary layer has been studied intensively, (see for reviews Bull 1967, 1996; Willmarth 1975). Bull (1967) observed that wall pressure fluctuations can be decomposed into two families: a large-scale (low-frequency) component and a small-scale (high-frequency) component. The frequency division between these two families is approximately at $f\delta^*/U_\infty = 0.07$. The small-scale component of wall pressure fluctuations was found to be associated with burst-sweep events near the wall region, traveling at 0.67 of the freestream speed (Thomas & Bull 1983). Other researches found similar values of 0.53..0.73 for the convective speeds (Dinkelacker, Hessel, Meier & Schewe 1977; Emmer-

ling 1973). The large-scale component was found to move 0.75..0.85 of the freestream speed (Dinkelacker *et al.* 1977; Farabee & Casarella 1991; Willmarth 1975). The stream-wise span of this large-scale mode is reported to be approximately 3 to $5\delta^*$ (Bull 1967; Dinkelacker *et al.* 1977). Overall, the low-frequency component was found to contribute 75% to the total level of pressure fluctuation (Bull 1967).

As was mentioned before, both the statistical model (4.6) and the vortical-structure model (4.11) give the correct scaling of optical aberrations versus the freestream Mach number, density and the boundary layer thickness. Also, if in the simple pressure-based model (4.11), the vortex radius is taken as the measured spanwise optical length, $a = \Lambda_z \sim \delta^*$, then using the value of the Gladstone-Dale constant $K_{GD} = 2.27 \cdot 10^{-4} \text{ m}^3 \text{ kg}^{-1}$ and the observed turbulence intensity of $t = 7\%$, the simple-model scaling (4.11) would give,

$$\text{OPD}_{\text{r.m.s.}} = 1.1 \cdot 10^{-5} \delta^* \frac{\rho}{\rho_{\text{SL}}} M^2, \quad (5.1)$$

which is close to the experimentally measured relation (4.12); and so is the prediction of the statistical model, which gives for the constant the value of approximately $2.0 \cdot 10^{-5}$. In addition, the statistical model provides the correct estimation of the average convective speed of the optical aberrations, as it was shown in Section 4.2.4.

But the statistical, SRA-based model alone, cannot properly explain the significant frequent intermittent increases in $\text{OPD}_{\text{r.m.s.}}$ and subsequent drop-outs in the far-field intensity, reported in Section 4.2.9. On the other hand, the vortical model inherently relies on the presence of compact vortical structures inside the outer region of the boundary layer and therefore properly predicts the origin of the intermittent intensity drop-outs.

Moreover, the simple vortical model also gives for the level of turbulent wall pressure fluctuations, normalized by the incoming dynamic pressure, q_∞ , to be $p_{\text{r.m.s.}}/q_\infty \approx 0.02$, which is close to the observed experimental values of $p_{\text{r.m.s.}}/q_\infty \approx 0.005$ to 0.008 for

$Re_\theta > 10^3$ (Bull 1967; Tsuji, Fransson, Alfredsson & Johansson 2007; Willmarth 1975). It should be further noted that if the simple model is valid, the r.m.s.-pressure values would be near the middle of the boundary layer and would be expected to be higher than those observed at the wall. The reason why the small-scale component does not contribute much to the overall optical distortions is that the optical aberration is an integral value and proportional to a structure amplitude multiplied by its size. Thus, although the small-scale-component amplitude is comparable to the large-scale component (Dinkelacker *et al.* 1977; Thomas & Bull 1983), its size is confined to the log-region of the boundary layer, which is small compared to the size of the large-scale component, which is of the size of the outer region.

All these observations provide strong, although indirect, evidence that the turbulent pressure fluctuations are the significant contributors to optical aberrations inside subsonic boundary layers. Further, the optical aberrations are also found to move at 0.81 of the freestream speed with the streamwise correlation length to be approximately $5\delta^*$.

It is worth mentioning that if one assumes that the pressure fluctuations are negligible, from the equation of state, it follows that the dependence of the density fluctuations is with the *inverse* of temperature, i.e., $\rho' \sim T'^{-1}$. But if the isentropic relation is assumed instead, $p \sim \rho^\gamma$, it leads to a positive relation between the density and temperature fluctuations, $\rho^{(\gamma-1)} \sim T'$. So, if one measures (or correctly computes) *independently* the static temperature and density/pressure variations inside the subsonic boundary layer, it would provide direct evidence of how static temperature and pressure fluctuations contribute to the optical aberrations in a turbulent boundary layer.

Finally, the clear suggestion that the Malley probe provides a valuable tool for investigating the fluid mechanics of turbulent boundary layers cannot be missed. The universal spectra curve (4.17), for example, provides a non-intrusive method of measuring the

boundary layer thickness. As long as the walls are reasonably adiabatic and the assumption of a fully-turbulent boundary layer can be made, locating the peak in the jitter spectra provides a robust measure of boundary layer thickness. Beyond this, the oblique-propagation angle dependence in the $OPD_{r.m.s.}$ calculation has provided presumptive evidence for the anisotropic orientation of structures in the outer region of the boundary layer. And, there are other suggestions for ways of making use of Malley probe data that can be gleaned from the data in this paper. Suffice to say, it is clear that the Malley probe offers a powerful new tool for investigating turbulent boundary layers.

REFERENCES

- ADRIAN, R. J. 2007 Hairpin vortex organization in wall turbulence. *Phys. Fluids* **19** (4), 1–16.
- ADRIAN, R. J., MEINHART, C. D. & TOMKINS, C. D. 2000 Vortex organization in the outer region of the turbulent boundary layer. *J. Fluid Mech.* **422**, 1–54.
- BUCKNER, A., GORDEYEV, S. & JUMPER, E. J. 2005 Optical aberrations caused by transonic attached boundary layers: underlying flow structure. In *43rd AIAA Aerospace Sciences Meeting and Exhibit*. Reno, NV, 10–13 January 2005, AIAA Paper 2005-0752.
- BULL, M. K. 1967 Wall-pressure fluctuations associated with subsonic turbulent boundary layer flow. *J. Fluid Mech.* **28** (4), 719–754.
- BULL, M. K. 1996 Wall-pressure fluctuations beneath turbulent boundary layers: some reflections on forty years of research. *J. Sound Vib.* **190** (3), 299–315.
- DERON, R., TROMEUR, E., AUPOIX, B. & DESSE, J. M. 2002 Rapport d’activités 2001 du projet de recherche fédérateur effets aéro-optiques. *Tech. Rep.* 4/06008. DOTA, ONERA, France.
- DINKELACKER, A., HESSEL, M., MEIER, G. E. A. & SCHEWE, G. 1977 Investigation of pressure fluctuations beneath a turbulent boundary layer by means of an optical method. *Phys. Fluids* **20** (10), S216–S224.
- DUMAS, J., FUQUA, M. & HAYDEN, T. 2005 Final report: boundary layer survey of the subsonic wind tunnel. *Tech. Rep.*. Department of Aeronautics, United States Air Force Academy.

- EMMERLING, R. 1973 The instantaneous structure of the wall pressure under a turbulent boundary layer. *Tech. Rep. 9*. Max-Planck-Institut für Strömungsforschung.
- FARABEE, T. M. & CASARELLA, M. J. 1991 Spectral features of wall pressure fluctuations beneath turbulent boundary layers. *Phys. Fluids A: Fluid Dynamics* **3** (10), 2410–2420.
- FITZGERALD, E. J. & JUMPER, E. J. 2004 The optical distortion mechanism in a nearly incompressible free shear layer. *J. Fluid Mech.* **512**, 153–189.
- GARINER JR., W. C., HIDAKA, Y. & TANZAWA, T. 1980 Refractivity of combustion gases. *Combust. and Flame* **40**, 213–219.
- GILBERT, G. K. 1982 Kc-135 aero-optical boundary-layer/shear-layer experiments. In *Aero-Optical Phenomena* (ed. G. K. Gilbert & L. J. Otten), *Progress in Astronautics and Aeronautics Series*, vol. 80, pp. 306–324. New York: AIAA.
- GILBERT, K. G. & OTTEN, L. J., ed. 1982 *Aero-Optical Phenomena, Progress in Astronautics and Aeronautics Series*, vol. 80. New York: AIAA.
- GLADSTONE, J. H. & DALE, T. P. 1863 Researches on the refraction, dispersion, and sensitiveness of liquids. *Philosophical Transactions of the Royal Society of London* **153**, 317–343.
- GORDEYEV, S., HAYDEN, T. & JUMPER, E. J. 2007 Aero-optical and flow measurements over a flat-windowed turret. *AIAA Journal* **45** (2), 347–357.
- GORDEYEV, S., JUMPER, E. J., NG, T. T. & CAIN, A. 2003 Aero-optical characteristics of compressible, subsonic turbulent boundary layers. In *34th AIAA Plasmadynamics and Lasers Conference*. Orlando, FL, 23–26 June 2003, AIAA Paper 2003-3606.
- GRANT, H. L. 1958 The large eddies of turbulent motion. *J. Fluid Mech.* **4**, 149–190.
- HUGO, R. J. & JUMPER, E. J. 1995 Quantification of aero-optical phase distortion using the small-aperture beam technique. *AIAA Journal* **33** (11), 2151–2157.
- HUTCHINS, N., HAMBLETON, W. T. & MARISIC, I. 2005 Inclined cross-stream stereo particle image velocimetry measurements in turbulent boundary layers. *J. Fluid Mech.* **541**, 21–34.
- JUMPER, E. J. & FITZGERALD, E. J. 2001 Recent advances in aero-optics. *Progress in Aerospace Sciences* **37** (3), 299–339.
- LIEPMANN, H. W. 1952 Deflection and diffusion of a light ray passing through a boundary layer. Report SM-14397. Douglas Aircraft Company, Santa Monica Division, Santa Monica, CA.

- MALLEY, M., SUTTON, G. W. & KINCHELOE, N. 1992 Beam-jitter measurements of turbulent aero-optical path differences. *Applied Optics* **31** (22), 4440–4443.
- MASSON, B., WISSLER, J. & McMACKIN, L. 1994 Aero-optical study of a nc-135 fuselage boundary layer. In *32nd AIAA Aerospace Sciences Meeting and Exhibit*. Reno, NV, 10-13 January 1994, AIAA Paper 1994-0277.
- MORKIVIN, M. V. 1962 Effects of compressibility on turbulent flows. In *Mechanique de la Turbulence* (ed. A. Farve), pp. 367–380. Paris, France: CNRS.
- NAGIB, H. M., CHAUHAN, K. A. & MONKEWITZ, P. A. 2005 Scaling of high reynolds number turbulent boundary layers revisited. In *4th AIAA Theoretical Fluid Mechanics Meeting*. Toronto, Ontario, Canada, 6-9 June 2005, AIAA Paper 2005-4810.
- ROBINSON, S. K. 1991 Coherent motions in the turbulent boundary layer. *Annual Review of Fluid Mechanics* **23** (1), 601–639.
- ROSE, W. C. 1979 Measurements of aerodynamic parameters affecting optical performance. Final Report AFWL-TR-78-191. Air Force Weapons Laboratory.
- ROSE, W. C., JOHNSON, D. A. & OTTEN, L. J. 1982 Summary of all cycle ii.5 aerodynamic shear- and boundary-layer measurements. In *Aero-Optical Phenomena* (ed. K. G. Gilbert & L. J. Otten), *Progress in Astronautics and Aeronautics Series*, vol. 80, pp. 294–305. New York: AIAA.
- SIEGENTHALER, J. P. 2008 Guidelines for adaptive-optic correction based on aperture filtration. PhD thesis, University of Notre Dame.
- SIEGENTHALER, J. P., GORDEYEV, S. & JUMPER, E. J. 2005 Shear layers and aperture effects for aero-optics. In *36th AIAA Plasmadynamics and Lasers Conference*. Toronto, Ontario, Canada, 6-9 June 2005, AIAA Paper 2005-4772.
- SMITH, W. J. 1966 *Modern Optical Engineering: The Design of Optical Systems*, chap. 3, pp. 49–71. New York: McGraw-Hill.
- STINE, H. A. & WINOVICH, W. 1956 Light diffusion through high-speed turbulent boundary layers. Research Memorandum A56B21. NACA, Washington, D. C.
- SUTTON, G. W. 1969 Effects of turbulent fluctuations in an optically active fluid medium. *AIAA Journal* **7** (9), 1737–1743.

- SUTTON, G. W. 1985 Aero-optical foundations and applications. *AIAA Journal* **23**, 1525–1537.
- TATARSKI, V. I. 1961 *Wave Propagation in Turbulent Medium*. New York: McGraw-Hill.
- THOMAS, A. S. W. & BULL, M. K. 1983 On the role of wall-pressure fluctuations in deterministic motions in the turbulent boundary layer. *J. Fluid Mech.* **128**, 283–322.
- TOMKINS, C. D. & ADRIAN, R. J. 2003 Spanwise structure and scale growth in turbulent boundary layers. *J. Fluid Mech.* **490**, 37–74.
- TROMEUR, E., GARNIER, E. & SAGAUT, P. 2006a Analysis of the sutton model for aero-optical properties of compressible boundary layers. *J. Fluid Eng.* **128** (2), 236–246.
- TROMEUR, E., GARNIER, E. & SAGAUT, P. 2006b Large-eddy simulation of aero-optical effects in a spatially developing turbulent boundary layer. *J. Turbulence* **7** (1), 1–27.
- TROMEUR, E., GARNIER, E., SAGAUT, P. & BASDEVANT, C. 2002 Les of aero-optical effects in turbulent boundary layer. In *Engineering Turbulence Modelling and Experiments 5* (ed. W. Rodi & N. Fueyo), pp. 327–336. Mallorca, Spain, 16–18 September 2002: Elsevier Science Ltd.
- TROMEUR, E., GARNIER, E., SAGAUT, P. & BASDEVANT, C. 2003 Large eddy simulations of aero-optical effects in a turbulent boundary layer. *J. Turbulence* **4**, 1–22.
- TRUMAN, C. R. 1992 The influence of turbulent structure on optical phase distortion through turbulent shear flows. In *AIAA and SDIO, Annual Interceptor Technology Conference*. Huntsville, AL, 19–21 May 1992, AIAA Paper 1992-2817.
- TRUMAN, C. R. & LEE, M. J. 1990 Effects of organized turbulence structures on the phase distortions in a coherent optical beam propagating through a shear layer. *Phys. Fluids* **2** (5), 851–857.
- TSUJI, Y., FRANSSON, J. H. M., ALFREDSSON, P. H. & JOHANSSON, A. V. 2007 Pressure statistics and their scaling in high-reynolds-number turbulent boundary layers. *J. Fluid Mech.* **585**, 1–40.
- VAN DYKE, M. 1982 *An Album of Fluid Motion*, p. 92. Stanford, CA: The Parabolic Press.
- WILLMARTH, W. W. 1975 Pressure fluctuations beneath turbulent boundary layers. *Annu. Rev. Fluid Mech.* **7** (1), 13–36.
- WITTICH, D. J., GORDEYEV, S. & JUMPER, E. J. 2007 Revised scaling of optical distortions

caused by compressible, subsonic turbulent boundary layers. In *38th AIAA Plasmadynamics and Lasers Conference*. Miami, FL, 25-28 June 2007, AIAA Paper 2007-4009.

WYCKHAM, C. M., ZAIDI, S. H., MILES, R. B. & SMITS, A. J. 2005 Measurements of aero-optic distortion in transonic and hypersonic, turbulent boundary layers with gas injection. In *36th AIAA Plasmadynamics and Lasers Conference*. Toronto, Ontario, Canada, 6-9 June 2005, AIAA Paper 2005-4755.